Defining a biogeochemical baseline for sediments at Carbon Capture and Storage (CCS) sites: an example from the North Sea (Goldeneye)

A. W. Dale[1], S. Sommer[1], A. Lichtschlag[2], D. Koopmans[3], M. Haeckel[1], E. Kossel[1], C. Deusner[1], P. Linke[1], J. Scholten[4], K. Wallmann[1], M. R. van Erk[3], J. Gros[1], F. Scholz[1], M. Schmidt[1]

[1] GEOMAR Helmholtz Centre for Ocean Research Kiel, Wischhofstrasse 1–3, 24148 Kiel, Germany.
[2]National Oceanography Centre Southampton, University of Southampton Waterfront Campus, European Way, Southampton SO14 3ZH, UK
[3]Max Planck Institute for Marine Microbiology, Celsiusstraße 1, Bremen, 28359, Germany
[4]Institute of Geosciences, Christian-Albrechts-Universität zu Kiel (CAU), Otto-Hahn-Platz 1, 24118 Kiel, Germany

Abstract

Injection of carbon dioxide (CO_2) into subseafloor reservoirs is gaining traction as a strategy for mitigating anthropogenic CO_2 emissions to the atmosphere. Yet, potential leakage, migration and dissolution of externally-supplied CO_2 from such reservoirs are a cause for concern. The potential impact of CO_2 leakage on the biogeochemistry of sediments and overlying waters in the North Sea was studied during a controlled subsurface CO_2 release experiment in 2019 at a potential carbon capture and storage site (Goldeneye). This study describes the natural (unperturbed) biogeochemistry of sediments. They are classified as muddy sand to sandy mud with low organic carbon content (~0.6 %). Distributions of dissolved inorganic carbon (DIC) and total alkalinity (TA) in sediment porewaters are reported in addition to in situ benthic fluxes of dissolved nutrients and oxygen between the sediments and the overlying water. Oxygen fluxes into the sediment, measured using benthic chambers and eddy covariance, were 6.18 ± 0.58 and 5.73 ± 2.03 mmol m^{-2} d^{-1}, respectively. Diagnostic indicators are discussed that could be used to detect CO_2 enrichment of sediments due to reservoir leakage at CCS sites. These include the ratio TA and ammonium to sulfate in sediment porewaters, benthic fluxes and chloride-normalized cation distributions. These indicators currently suggest that the organic carbon at Goldeneye has an oxidation state below zero and is mainly degraded via sulfate reduction. Carbonate precipitation is apparently negligible, whereas decreases in Mg^{2+} and K^+ point toward ongoing alteration of lithogenic sediments by reverse weathering processes.

Keywords: biogeochemistry, sediment, fluxes, CCS, alkalinity, CO_2, reverse weathering, North Sea

1. Introduction

The uncontrolled emission of CO_2 to the atmosphere is enhancing the global greenhouse effect and ocean acidification (IPCC, 2014). In an attempt to tackle this problem, attention is being focused on offsetting anthropogenic CO_2 emissions by capturing CO_2 at points of emission and sequestering it in deep subsurface sedimentary reservoirs onshore and offshore, so-called Carbon Capture and Storage (CCS). For various reasons, one of them being the high costs of CO_2 capture and storage (about 50 – 100 €/t, (Acatech, 2018)) and the low emission certificate prices in the EU Emissions Trading system (about 25 €/t in 2020), CCS has not been implemented at large scale in Europe even though most projections show that the climate targets (<2.0°C global warming) cannot be reached without CCS (IPCC, 2005; 2018). However, this situation may change in the near future due to the growing public pressure to implement climate change mitigation policies and more stringent conditions in the 4th EU trading period for emission certificates (2021 to 2030).

Potential leakage of CO_2 from offshore CCS sites remains an environmental concern (Dixon and Romanak, 2015). Consequently, strong efforts are needed to determine an effective environmental baseline in order to provide the data needed to discriminate the potential direct signals of unintended CO_2 leakage from CCS sites from those caused by other natural or man-made drivers (e.g. Blackford et al., 2015; Wallmann et al., 2015). Given the natural heterogeneity of marine systems, the potential for reading false positive and negative signals of CO_2 leakage from field data is high (Blackford et al., 2015).

The sedimentary overburden above a potential CO_2 storage site in the North Sea, known as Goldeneye, was targeted in the framework of the Horizon 2020 project STEMM-CCS of the EU (*Strategies for Environmental Monitoring of Marine CCS*; www.stemm-ccs.eu). The main goal of STEMM-CCS is to develop and test strategies and technologies for the detection, attribution and quantification of seabed leakage from subseafloor CO_2 storage operations. In this context, a small research-scale CO_2 release experiment began on 11 May 2019 at Goldeneye. A controlled release of 675 kg of gaseous CO_2 was undertaken until 22 May by injecting pressurized CO_2 about 3 m below the sediment surface through a pipe (STEMM-CCS project consortium, 2020; Flohr et al., this issue). Gas release resulted in CO_2 bubble streams rising from the seafloor and a change in biogeochemical properties of the sediments from the natural environmental baseline (Lichtschlag et al., this issue). A similar experiment undertaken in a Scottish bay showed that CO_2 injection in sediments promotes the dissolution of carbonate and silicate minerals and the release of trace metals (Lichtschlag et al., 2015; Taylor et al., 2015). A reduction in the pH of interstitial pore waters and liberation of trace metals may be detrimental to marine fauna dwelling in or on the seabed (e.g. De Orte et al., 2014; Lessin et al., 2016).

In the event of CO_2 leakage, the extent and persistence of CO_2 enrichment in sediments may need to be determined. However, the dissolution of external CO_2, possibly in low amounts, may have a similar geochemical signature as that due to naturally-occurring anaerobic degradation of organic matter. The aim of this study, therefore, is to describe the biogeochemical state of sediments at Goldeneye that are unaffected by the release experiment in order that the impact of CO_2 release on benthic biogeochemistry can be easily detected and quantified. Data including dissolved and particulate chemical components, in situ benthic flux measurements using incubation chambers and eddy covariance techniques, and rates of sediment mixing by animals (bioturbation and bioirrigation) were collected over several research campaigns. Based on those measurements, we examined organic carbon degradation and burial, biogeochemical zonation in sediments, and the stoichiometry of organic matter remineralization. The data are used to derive a number of general diagnostic indicators for detecting CO_2 release from offshore CCS sites. A baseline study of water column biogeochemistry at Goldeneye has been reported by Esposito et al. (this issue).

2. Study area

Goldeneye is a depleted gas field and platform in the northern North Sea, ~100 km NE of Peterhead (Scotland) that was operated by Shell from 2004 until 2011 (Fig. 1). The seafloor in the region is relatively flat and gently sloping deeper in a north-easterly direction with a water depth in the vicinity of the platform of around 120 m. Seafloor terrain includes relict moraines from the last ice age, glacial lineations and iceberg ploughmarks. Sediments at Goldeneye are poorly sorted with a major mode grain size of ~63 µm. Sediment accumulation rates determined in the wider area range from 0.05 to 0.35 cm yr^{-1} (de Haas et al., 1997). Sediments in the upper 1 – 15 m of the seafloor comprise the Witch Ground Formation that was deposited after the retreat of grounded ice ca. 27 kyr BP (Marine Isotope Stage 1-2, Böttner et al., 2019). The Witch Ground Formation at Goldeneye is 4 - 7 m thick and overlies the Witch Ground Graben (Böttner et al., 2019; Connelly, 2019). Pockmarks ranging from ~6 to 460 m in diameter and up to 18 m in depth are numerous in the area (Long, 1992; Judd et al., 1994). The larger Class 1 pockmarks (>100 m in diameter) are fed by deep gas from Mid-Pleistocene glaciogenic units and sites of active gas venting (Böttner et al., 2019). The far more numerous, yet smaller, Class 2 pockmarks (<100 m in diameter) are believed to be relict (Shell, 2014; Böttner et al., 2019). Tides, seasonality and storm events dominate the hydrographical structure in the water column and short-term variations in carbonate system parameters (Esposito et al., this issue).

3. Methods

3.1 Sediment sampling

The positioning of the sediment sampling devices is shown in Fig. 1. Sediment cores were taken in October 2017, August 2018 and May 2019 during three research campaigns on board RV Poseidon; POS518, POS527 and POS534, respectively (Table 1). The CO_2 injection experiment began on 11 May 2019 and ended on 22 May 2019. It was conducted by scientists on board RRS James Cook, cruise JC180 (Flohr et al., this issue). Sampling during cruise POS534 took place immediately after the CO_2 injection was stopped. The physical and geochemical properties of these sediments were virtually identical to those on earlier cruises, presumably because the cores were taken too far from the CO_2 bubble streams (3 – 7 m away) to be affected by them. We consider all the data presented in this study as baseline values and unaffected by the CO_2 injection. Sediment data taken in the immediate vicinity of the CO_2 bubble streams are presented by Lichtschlag et al. (this issue).

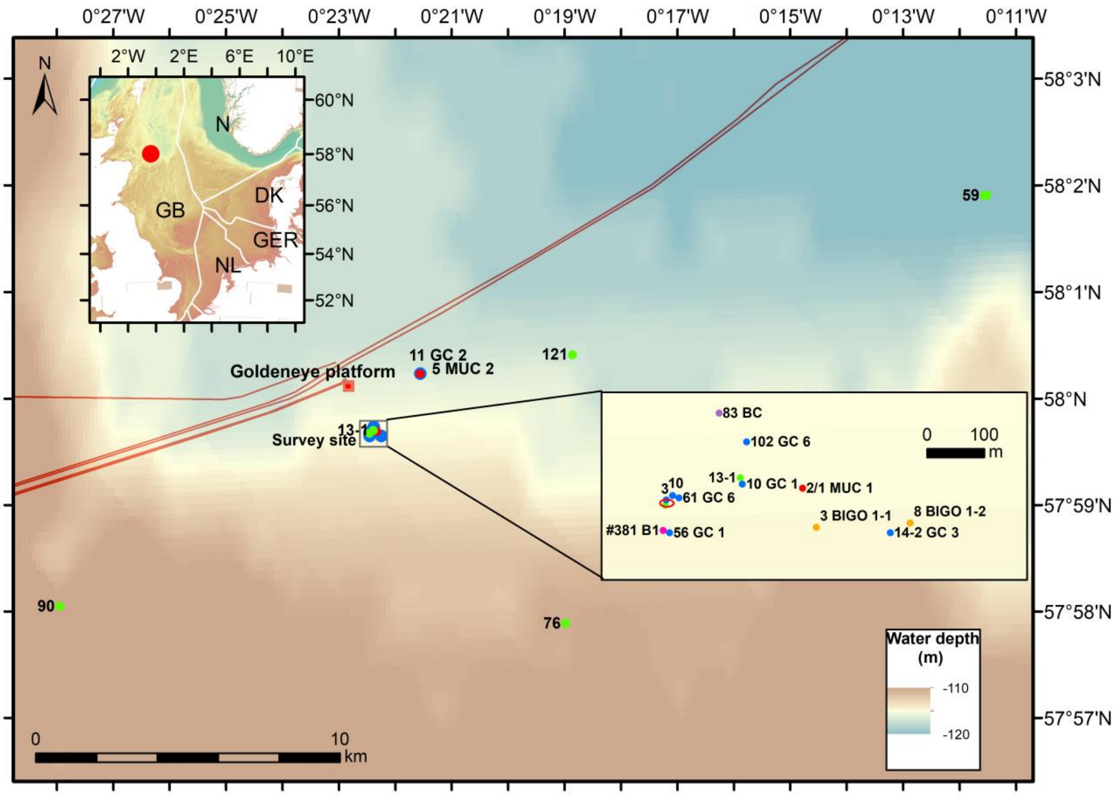

Fig. 1. Study area at the Goldeneye site and location of the platform. Sampling instruments described in Table 1 and 2 are labelled and colored red (multiple-corer, MUC), blue (gravity core, GC), orange (landers, BIGO), green (eddy covariance, EC), purple (box corer, BC) and pink (Remotely Operated Vehicle, ROV). The lines denote pipelines. The inset shows the location of study area in the northern North Sea.

Undisturbed surface sediments discussed in this study were sampled using a multiple-corer (MUC, POS518), a box-corer (BC, POS527) and by a Remotely Operated Vehicle (ROV) using push cores (JC180, ROV dive #381).

Up to eight sediment cores can be collected with each MUC deployment in transparent Perspex liners (60 cm long, 10 cm inner diameter). Due to the silty nature of the sediment, penetration did not exceed ca. 25 cm. Recovered sediments were immediately processed on board by sectioning under ambient air with a depth resolution ranging from 1 cm at the surface to 4 cm in the deeper part of the cores. Porewater was extracted by squeezing the sediment under gas pressure (4 bar) and filtering (0.2 µm cellulose acetate). Remaining sediments were stored at 4 °C for geochemical analysis of solid phases in the home laboratory (GEOMAR).

Surface sediments from the BC were sampled by inserting Perspex liners (40 cm long, 8 cm inner diameter) into the sediment ('push cores') on deck. Push cores also were taken in Perspex liners (30 cm long, 8 cm inner diameter) by the ROV launched from the James Cook (JC180). The location of the background coring site was ~50 m from the injection site where gas bubbling was visible.

Longer sediment cores up to 4 m were retrieved with a gravity corer (GC) on POS518 and POS534. On retrieval, the inner plastic liner (11 cm inner diameter) was cut into 1-m long segments. Each segment was cut lengthwise into a sampling half and an archive half. The solid phase was sampled and porewater was extracted in the same way as described above at sampling intervals of 20 – 30 cm. The sampling and the archive halves were transferred into protective cases (D-tubes) for long-term storage (4°C) at GEOMAR's refrigerated core repository. An additional core (GC6) was taken in August 2018 (POS527) and subsampled through drilled holes in the core liners every 20 cm down to 450 cm of the Witch Ground Formation. Sediments for the analysis of stable particulate carbon isotopes and particle grain size from GC6 were stored at -20°C and 4°C, respectively, until analysis at the National Oceanography Centre (UK). The GC data have not been corrected for the loss of surface sediment (typically 1 – 2 dm) resulting from the penetration of the core barrel through the sediment. GC sample depths are thus distance from the top of the recovered sediment.

Table 1. Sampling details for the Biogeochemical Observatory (BIGO), multiple-corer (MUC), gravity corer (GC), box core (BC), and Remotely Operated Vehicle (ROV) at background sites discussed in this work.[a]

Deployment device and number	Campaign	Water depth (m)	Date (2017)	Lat. (°N)	Long. (°W)	Core length (cm)
10 GC 1	POS518	116	30.09.17	57° 59.694'	00° 22.387'	299
11 GC 2	POS518	117	30.09.17	58° 00.233'	00° 21.555'	287
2/1 MUC 1	POS518	115	16.10.17	57° 59.69'	00° 22.330'	30
5 MUC 2	POS518	120	18.10.17	58° 00.23'	00° 21.560'	22
14-2 GC-3	POS518	117	20.10.17	57° 59.648'	00° 22.247'	435
102 GC 6 [b,c]	POS527	116	29.08.18	57° 59.734'	00° 22.383'	530
83 BC Lander [b,d]	POS527	114	28.08.18	57° 59.761'	00° 22.409'	19
ROV381 B1 [b]	JC180	117	26.05.19	57° 59.650'	00° 22.462'	20
56 GC 1	POS534	117	25.05.19	57° 59.648'	00° 22.456'	407
58 GC 3	POS534	117	25.05.19	57° 59.679'	00° 22.459'	429
61 GC 6	POS534	117	26.05.19	57° 59.681'	00° 22.447'	409
65 GC 10	POS534	117	26.05.19	57° 59.683'	00° 22.453'	420
3 BIGO 1-1	POS518	117	16.10.17	57° 59.653'	00° 22.317'	-
8 BIGO 1-2	POS518	115	19.10.17	57° 59.657'	00° 22.228'	-

[a] Cruise reports and complete station lists are provided in the references: POS518: Linke and Haeckel (2018); POS527: Achterberg and Esposito (2018); POS534: Schmidt (2019); JC180: Connelly (2019)

[b] For sulfate reduction rate measurements

[c] For grain size and $\delta^{13}C$ analyses

[d] Box core sampled at the Develogic Lander site (Esposito et al., this issue)

3.2 In situ benthic flux determinations

3.2.1 Benthic incubation chambers

Benthic fluxes of solutes were determined at two sites in the Goldeneye area during POS518 (Table 1) from time-series data collected in situ using a BIGO lander (Biogeochemical Observatory). The lander has been described in detail by Sommer et al. (2016). Each BIGO contained two circular flux chambers (internal diameter 28.8 cm; surface area 651.4 cm^2). A video-guided launching system allowed smooth placement of the observatories at selected sites on the sea floor. About 1 hour after the program of the observatory was started on deck, the chambers were slowly driven into the sediment (~ 30 cm h^{-1}) to an insertion depth of ~13 cm and a final height of water in the chambers of 20 – 22 cm. A mechanical stirrer gently mixed overlying water within the chamber without resuspension of sediment for an incubation time of ~36 h. Eight sequential water samples were removed from each chamber at discrete time intervals with glass syringes (volume ~ 47 ml) mounted to autosampler racks. Another eight water samples were taken for the analysis of N_2/Ar in quartz glass tubes (Sommer et al., 2016). Solute fluxes were calculated from the change in concentration over time and the height of the overlying water in each chamber. Positive fluxes are directed into the sediment and vice versa. Benthic fluxes determined using benthic chambers integrate the total solute exchange due to molecular diffusion and through flushing of animals burrows (bioirrigation, see below). To monitor the ambient bottom water geochemistry an additional series of eight glass tubes were sampled outside of the chambers.

Dissolved O_2 was measured inside the chambers and in the ambient seawater using optodes (Aanderaa). These were calibrated based on the O_2 time series recorded by an additional benthic lander that was deployed from 16 – 22 October 2017. Dissolved O_2 data recorded by this lander were calibrated using CTD/water sampling rosette casts. The flux of dissolved O_2 into the sediment determined with the benthic chambers is reported as total oxygen uptake (TOU_{BC}) with a positive sign. Benthic O_2 production by photosynthetic microalgae is assumed to be zero at this water depth in the North Sea (120 m).

3.2.2 Eddy covariance

Benthic fluxes of dissolved O_2 were determined with the aquatic eddy covariance (EC) technique at Goldeneye in September 2017 (POS518), August 2018 (POS527) and May 2019 (JC180, Table 2). Turbulence is the mechanism responsible for the vertical mixing of solutes through the benthic boundary layer (Boudreau et al., 2001). EC determines solute fluxes as the covariance of high frequency (e.g., 5 Hz) observations of vertical velocity and solute concentration (Berg et al., 2003). Turbulent fluctuations in water velocity and solute concentration were made 16 cm above the sediment surface, yielding a contributing flux footprint of tens of meters squared directly upstream of the instruments (Berg et al., 2007).

High frequency oxygen concentrations were measured with a minisensor optode (PyroScience, GmbH). The optode was calibrated in O_2-saturated and anoxic water (a pH buffered sodium ascorbate solution) prior to deployment. The analog oxygen signal was recorded by the acoustic Doppler velocimeter (Nortek-AS). Eddy covariance equipment was mounted to an aluminum lander and deployed by winch during POS527. The equipment was mounted to a lightweight fiberglass frame and deployed by ROV during POS518 and JC180. Baseline EC measurements during campaign JC180 took advantage of tidal oscillations in the current direction to determine benthic uptake over minimally disturbed sediments on the opposite side of EC instruments from the point of CO_2 release.

EC fluxes were calculated in half-hour intervals following the procedure described by Holtappels et al. (2013). Briefly, the tilt of the acoustic Doppler velocimeter was corrected using the planar fit method by Wilczak et al. (2001). A running average with a window of 300 s was subtracted from the time series to calculate the fluctuating components of vertical velocity and concentration. The time lag between observation of velocity and the observation of solute concentration was accounted for by aligning the time series at the maximum cross-correlation coefficient. The median resulting time shift of O_2 was 0.8 s. Benthic flux of dissolved O_2 into the sediment determined by EC is reported as total oxygen uptake (TOU_{EC}) with a positive sign.

Table 2. Eddy covariance oxygen flux measurement dates, times (midpoint), and location. The duration was from 0.5 h (13-1) to 26 h (1-4) with a mean of 9.6 h.

Station	Campaign	Water depth (m)	Date (2017)	Time (UTC)	Lat. (°N)	Long. (°W)
13-1	POS518	116	30.09.17	14:00	57° 59.700'	00° 22.389'
55	POS527	129	23.08.18	06:39	58° 01.904	00° 11.516'
59	POS527	125	24.08.18	14:09	58° 01.904	00° 11.561'
76	POS527	119	26.08.18	15:16	57° 57.889	00° 18.983'
90	POS527	114	29.08.18	07:21	57° 58.048	00° 27.950'
121	POS527	125	30.08.18	15:13	58° 00.411	00° 18.860'
1-2	JC180	116	13.05.19	15:30	57° 59.674	00° 22.460'
1-4	JC180	116	21.05.19	15:40	57° 59.674	00° 22.460'

3.3 Sediment analysis

Geochemical analyses of the porewaters and sediments at Goldeneye aimed at quantifying the biogeochemical fluxes and turnover rates associated with organic carbon remineralization. Porewater analyses of the following parameters were carried out onboard: nitrate (NO_3^-), nitrite (NO_2^-), ammonium (NH_4^+), total dissolved phosphate (PO_4^{3-}), silicic acid (H_4SiO_4), total dissolved hydrogen sulphide (H_2S) and total alkalinity (TA). NO_3^-, NO_2^-, NH_4^+, PO_4^{3-}, and H_4SiO_4 were determined using standard methods on a Quaatro Autoanalyzer (Seal Analytic) (Grasshoff et al., 1999) or on a spectrophotometer (Hitachi U-2001 or U-5100). The two instruments showed an agreement to within 5 %. All samples from the BIGO syringes for nutrient analysis were determined using the autoanalyzer. Samples for TA were analyzed by titration of 0.5-1 ml of porewater (cores) or 1-2 ml bottom water (lander syringes) using a color indicator according to Ivanenkov and Lyakhin (1978) and HCl as titrant. Titration was ended when a stable pink colour appeared. During titration, the sample was degassed by continuously bubbling nitrogen to remove any generated CO_2 and H_2S. The procedure was standardized using an International Association for the Physical Sciences of the Oceans

(IAPSO) seawater solution. Analytical precision and detection limits of each method are given in the POS518 cruise report available online (Linke and Haeckel, 2018).

Untreated filtered samples were also stored refrigerated for onshore analysis of chloride (Cl^-), bromide (Br^-), and sulfate (SO_4^{2-}), by ion-chromatography. Acidified sub-samples (30 µl suprapure HNO_3^- + 3 ml sample) were prepared for analyses of major ions (K^+, Li^+, Mg^{2+}, Ca^{2+}, Sr^{2+}, Br^-, and I^-) by inductively coupled plasma optical emission spectroscopy (ICP-OES) at the home laboratory (GEOMAR). The analytical precision was 2 – 5 %. Dissolved Fe and Mn were also determined by ICP-OES and represent the total dissolved fractions in their various oxidation states (DFe_T and DMn_T). Although the samples were processed as fast as possible, loss of dissolved Fe^{2+} and Mn^{2+} by aerobic oxidation and precipitation as Fe(III) and Mn(IV) is inevitable. We thus treat the DFe_T and DMn_T data qualitatively as indicators for the iron- and manganese-reducing layers in the sediment.

Wet sediment samples (~5 ml) for analysis of particulate organic carbon (POC), particulate organic nitrogen (PON) and total sulfur (S_T) were freeze–dried in the home laboratory and analyzed using a Euro elemental analyzer. POC content was determined after acidifying the sample with HCl (0.25 N) to transform the inorganic components to CO_2. Weight percent of total carbon was determined using samples without acidification. Particulate inorganic carbon (PIC, in weight % C), assumed to be calcium or magnesium carbonates, was determined by weight difference between total and organic carbon. The precision and detection limit of the POC analysis was 0.04 and 0.05 dry weight percent (% C), respectively, while that for inorganic carbon was 2 and 0.1 % C. Water content was determined from the weight difference of the wet and freeze–dried sediment. Values were converted to porosity (water volume fraction of total sediment) assuming a dry sediment density of 2.5 g cm^{-3} and seawater density of 1.023 g cm^{-3}.

The stable carbon isotope ($\delta^{13}C$) ratios of carbon were determined in GC6 (POS527) with a Thermo Fisher Scientific Flash 2000 Elemental Analyser (EA) coupled to a Delta V Advantage Isotope ratio mass spectrometer (IRMS) via a ConFlo IV Continuous Flow interface. For organic carbon analysis, the inorganic carbon was first removed with 10% phosphoric acid. The grain size of the sediment was determined in this same core as the average of ten measurements per sample (standard deviation (SD) < 3%) with a Malvern Mastersize 3000 after shaking overnight in distilled water to disaggregate them.

Total iron (Fe_T), manganese (Mn_T) and aluminum (Al) concentrations in the solid phase were determined by ICP-OES following digestion of dried and ground sediment samples in nitric acid, hydrofluoric acid and perchloric acid. For quality control, the Certified Reference Material MESS-3 (marine sediment, Canadian Research Council) was digested and analyzed along with sediment samples. The obtained values were always within the certified ranges.

A sequential sediment extraction for the recovery of highly reactive Fe phases was applied to the freeze-dried and ground sediment samples (Poulton and Canfield, 2005). In brief, Fe bound to carbonate minerals (Fe_{carb}) was extracted with sodium acetate, Fe bound to (oxyhydr)oxide minerals (Fe_{ox}) was extracted with sodium dithionite and Fe bound to magnetite (Fe_{Mag}) was extracted with ammonium oxalate. Extraction solutions were analyzed for Fe concentration by ICP-OES with yttrium as an internal standard. Fe bound to pyrite (FeS_2, Fe_{py}) was determined by the chromium reduction method (Canfield et al., 1986). The sum of these four fractions represents the highly reactive Fe pool (Fe_{HR}).

3.5 Sulfate reduction rates (SRR)

Sediments retrieved on POS527 and JC180 were sampled for sulfate reduction rate (SRR) measurements by radiotracer incubation (Table 1). The gravity core (GC6, POS527) was subsampled in duplicate at the following depths: 0, 25, 50, 75, 100, 125, 150, 200, 300, 400 cm. The box core (POS527) and ROV push core (JC180) were sampled using push cores (2 replicates) at depths of 1, 2, 4, 8 and 16 cm. Sediments were collected in 5 ml cut-off syringes and immediately sealed with a black stopper and stored in a N_2-flushed zipper bag. Silicon tubing filled with 10 ml 1 M Na-ascorbate (pH 11) was placed in each zipper bag as an oxygen-trap. The samples were stored and transported at 0 – 4 ^{o}C until analysis at the home laboratory (Max Planck Institute for Marine Microbiology). In the laboratory, 50 kBq $^{35}SO_4^{2-}$ in 50 µL was injected past the black stoppers, taking care that the tracer was evenly distributed in the sediment. After >12 hours incubation, the samples were fixed in 20% (w/v) ZnAc and stored at -20 ^{o}C until cold acidic Cr^{2+} distillation and scintillation counting as described previously (Røy et al., 2014). The detection limit for the analysis was 0.03 nmol cm^{-3} d^{-1} (POS527) and 0.01 nmol cm^{-3} d^{-1} (JC180). All data reported here exceed these values.

3.5 Bioirrigation experiments

Solute exchange across the sediment-water interface due to the activity of burrowing organisms was determined on board by the addition of bromide as a dissolved conservative tracer to three sediment cores from the MUC casts; 2 from 2/1 MUC 1 (Cores D and K) one from 5 MUC 2 (Core M). The height of the overlying water was 33 cm (core D), 34 cm (core K) and 32 cm (core M). After adding the bromide (as NaBr) to a concentration of approximately 20 mM in the overlying water, the sediment cores were fitted with a loose-fitting stirrer head and incubated on board for a period of 5 - 6 days on the ship's deck in darkness at ambient temperature. At the end of the incubation, the sediment was sliced and porewater bromide concentrations were determined. These data were used to calculate bioirrigation rates with a time-dependent numerical model that simulated bromide infiltration into the sediment due to diffusion and bioirrigation over the incubation period. Full details of the model are described by Dale et al. (2013).

The change in bromide in sediment porewater (Br^-) resulting from bioirrigation was calculated with the model as:

$$\varphi \frac{\partial \mathrm{Br}^-}{\partial t} = \alpha_{bi} \varphi (\mathrm{Br}_{\mathrm{olw}} - \mathrm{Br}^-) \qquad (1)$$

where t is time, α_{bi} is the depth-dependent bioirrigation coefficient describing solute pumping through animal burrows with units of inverse time, and $\mathrm{Br}_{\mathrm{olw}}$ is the time-dependent Br^- concentration in the well mixed, overlying water. The sediment porosity, φ, was considered using a depth-dependent empirical function assuming steady–state compaction:

$$\varphi(x) = \varphi(\mathrm{L}) + (\varphi(0) - \varphi(\mathrm{L})) \cdot \exp\left(-\frac{x}{z_{por}}\right) \qquad (2)$$

where $\varphi(0)$ is the porosity at the sediment–water interface, $\varphi(L)$ is the porosity of compacted sediments and z_{por} is the length attenuation coefficient. These parameters were determined from the measured porosity data at each station.

α_{bi} was described as:

$$\alpha_{bi} = \alpha_1 \frac{\exp(\alpha_2 - x)}{1 + \exp(\alpha_2 - x)} \tag{3}$$

where α_1 is approximately equal to the bioirrigation coefficient at the sediment surface and α_2 is a length parameter that controls the irrigation depth. Numerical solutions for Br^- were obtained using the solver NDSolve in MATHEMATICA 11 employing Br_{olw} as the upper boundary condition and a zero gradient (Neumann) condition at the lower boundary (30 cm). Initial Br^- concentrations in the sediment were set to the ambient seawater values (825 uM) whilst Br_{olw} at $t = 0$ was set to the measured value in the water at the start of the incubation. The two irrigation parameters were constrained by fitting the model to the measured Br^- concentrations measured in the sediment porewaters at the end of the incubation period based on an ensemble of model simulations (2000 runs) in which the parameters were allowed to vary randomly. The best-fit parameters were chosen as the average of the ten best simulations with minimum least squares regressions between the measured and modeled result.

3.6 Sediment accumulation rates and bioturbation

Particle-bound unsupported ^{210}Pb ($^{210}Pb_{xs}$, half-life 22.3 yr) produced by the decay of ^{222}Rn in the sediment is subject to mixing in the upper sediment layers by the movement of benthic fauna as well as downward transport by ongoing sediment accumulation. The distribution of $^{210}Pb_{xs}$ can be used to determine sediment accumulation rates and biodiffusion coefficients (bioturbation) using a steady-state reaction-transport model that includes terms for describing the fluxes of $^{210}Pb_{xs}$ by sediment burial, mixing (bioturbation), compaction and radioactive decay of $^{210}Pb_{xs}$ (Alperin et al., 2002).

$^{210}Pb_{xs}$ was measured in samples from 2/1 MUC 1 and 5 MUC 2. For the analytical determination of ^{210}Pb, two high-purity coaxial Germanium detectors were used (CANBERRA BE3830P). Ground samples (~5-15g) were placed and sealed in a counter-specific calibrated plastic disc geometry and allowed to equilibrate for at least three weeks. ^{210}Pb was measured via its gamma peak at 46.5 keV. Detector efficiencies were determined using RGU-1, IAEA-375 and IAEA-385 certified reference materials. The evaluation of the gamma spectra, the calculations of radionuclide activities and associated uncertainties were performed using the ScienTissiME software (http://www.scientissime.net/). $^{210}Pb_{xs}$ was estimated by subtracting the supported ^{210}Pb (estimated from ^{214}Pb at 352 keV and ^{214}Bi at 610 keV) from the total $^{210}Pb_{xs}$ and is reported in Bq g^{-1}. No discernible differences in the depth distribution of $^{210}Pb_{xs}$ in the two cores could be observed and the two data sets were pooled for further analysis with the model.

Using the numerical model described above, $^{210}Pb_{xs}$ data were simulated with the following mass conservation equation (Dale et al., 2015):

$$\varepsilon\cdot\rho\cdot\frac{\partial\,^{210}\mathrm{Pb_{xs}}}{\partial \mathrm{t}}=\frac{\partial\left(\varepsilon\cdot\rho\cdot D_B(0)\cdot\exp\left(-\frac{x^2}{2\cdot x_B{}^2}\right)\cdot\frac{\partial\,^{210}\mathrm{Pb_{xs}}}{\partial \mathrm{x}}\right)}{\partial \mathrm{x}}-\frac{\partial\left(\rho\cdot\omega_{acc}\cdot(1-\varphi(L))\cdot{}^{210}\mathrm{Pb_{xs}}\right)}{\partial \mathrm{x}}+\varepsilon\cdot\rho\cdot\lambda\cdot{}^{210}\mathrm{Pb_{xs}} \qquad (4)$$

where ω_{acc} corresponds to the sediment accumulation rate of compacted sediments, ε is the depth-dependent solid volume fraction (i.e. $1-\varphi$), $D_B(0)$ is the bioturbation coefficient at the sediment–water interface, x_B approximates the bioturbation halving depth, λ (0.03114 $\mathrm{yr^{-1}}$) is the decay constant for $^{210}\mathrm{Pb_{xs}}$ and ρ is the bulk density of solid particles (2.5 g $\mathrm{cm^{-3}}$). The porosity function in Eq. (2) was used to define sediment compaction.

The flux of $^{210}\mathrm{Pb_{xs}}$ to the sediment surface, F(0), was determined from the measured integrated activity of $^{210}\mathrm{Pb_{xs}}$ multiplied by λ:

$$\mathrm{F}(0)=\lambda\cdot\rho\int_0^\infty {}^{210}\mathrm{Pb_{xs}}\cdot\varepsilon\,dx \qquad (5)$$

A zero gradient (Neumann) condition was imposed at the lower boundary (50 cm). The model was initialized using constant values for $^{210}\mathrm{Pb_{xs}}$ in the sediment column determined from the upper boundary flux. The model was solved for $D_B(0)$ and ω_{acc} after fixing x_B to 5 cm. This number was based on the bioirrigation experiment results and observed animal burrows. The parameters were constrained by fitting the model to the measured $^{210}\mathrm{Pb_{xs}}$ data, again using an ensemble of model simulations (2000 runs) in which the parameters were allowed to vary randomly. The best-fit parameters were chosen as the average of the ten best simulations with minimum least squares regressions between the measured and modeled result.

4. Results

4.1 Physical properties

The sediments are unimodal, poorly sorted muddy sand in the upper 40 cm and sandy mud from 40 to 450 cm. The mud content (<63 µm) at the surface was 33 %, increasing to 75 % at 120 cm, and from there increased gradually to 81 % at 450 cm (Fig. 2). No gravel was present.

In the short cores, sediment porosity decreased from 0.65 at the surface to ~0.5 at 5 cm (Fig. 3). In the long cores, porosity decreased steadily to ~0.4 by 100 cm depth and then increased again to almost 0.6 by 300 cm.

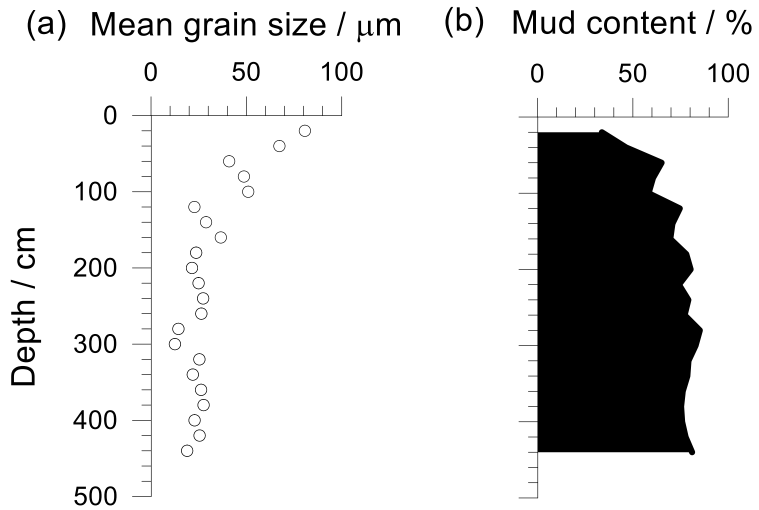

Fig. 2. (a) Median particle grain size (D_{50}, µm) and (b) mud content in core GC6 at Goldeneye.

4.2 Sediment geochemistry

Dissolved and particulate geochemical profiles from Goldeneye are shown in Fig. 3. POC and PON contents showed bi-model trends with depth in the sediment. Surface POC and PON contents were 0.6 and 0.1 wt.%, respectively, with mean values in the short cores of 0.53 and 0.08 %. Both properties had decreased by roughly one-third at ca. 100 cm. POC and PON then increased to near-surface values by 250 cm, and then decreased again until the bottom of the core. Organic matter was characterized by carbon-to-nitrogen ($r_{C:N}$) atomic ratios that increased monotonically from 7.5 at the surface to 10.2 at 400 cm. Mean $r_{C:N}$ over the whole data set was 8.5. The organic matter was thus depleted in N compared to phytoplankton with classical Redfield stoichiometry with a $r_{C:N}$ of 6.6 ($C_{106}H_{263}O_{110}N_{16}P$, Redfield et al., 1963). Particulate inorganic carbon (PIC, wt.% C) content decreased with depth from ~1.8 % at the surface to 0.8 % by 400 cm. δ^{13}C-POC varied from -23 to -25 ‰ relative to the standard (V-PDB) with a mean of -23.7 ‰. δ^{13}C-PIC averaged -2.1 ‰; a typical value for carbonates precipitated by marine organisms (Zeebe and Wolf-Gladrow, 2001).

Total iron (Fe_T) content in the short cores was around 1 %. Fe in the highly reactive pool (Fe_{HR}) was ~0.2 %. Iron (oxyhydr)oxide (Fe_{ox}) was ~0.07 % and showed little change with depth (not shown). Fe_{py} content was low, increasing from around 0.01 % (Fe) at the surface to 0.07 % at 24 cm, with an average of 0.03 %. The extent of pyritization (Fe_{py}/Fe_{HR}) increased steadily from 0.1 to 0.3. The mean Fe/Al ratio over the short cores was 0.33, which is lower than the crustal average of 0.44. Total S (S_T) was relatively low in the upper 40 cm with a mean content of 0.03 %, such that pyrite-S can account for the total S in the short cores. At greater depth, S_T increased to 0.5 % at 200 cm and then decreased to background levels. Mn oxides were not determined, but total Mn (Mn_T) was ~0.02 %.

DIC and TA concentrations in the short cores increased by ca. 0.1 mM and 0.2 mM above bottom water concentrations of 2.2 mM and 2.3 mM, respectively. Between ca. 100 and 130 cm depth in the long cores, DIC concentrations increased markedly to 5 - 6 mM and then remained roughly constant down to 400 cm. Similar changes were observed in TA and NH_4^+, concurrent with a decrease in SO_4^{2-}. Concentrations of H_2S remained mostly below detection limit in the short cores, increasing to only 3 µM in the long cores. Concentrations of Ca^{2+} decreased barely by < 1 mM throughout the sediment, whereas Mg^{2+} showed a stronger decrease of 6 – 7 mM.

Maximum concentrations of NO_3^- at the first data point below the sediment surface (0.5 cm) were 20 µM and higher than bottom water concentrations (~10 µM). NO_3^- then decreased down to the detection limit (~1 µM) by 4 – 5 cm. Concentrations of NO_2^- (not shown) were always < 1 (µM). Total dissolved Fe (DFe_T) was elevated in the upper 15 cm with maximum concentrations of 12 µM. Below this depth Fe^{2+} was generally < 5 µM. Total dissolved Mn (DMn_T) concentrations were < 3 µM in the short cores and < 1 µM at 50 cm in the long cores. DMn_T concentrations then increased gradually to 4 µM by 400 cm. It should be remembered that the DFe_T and DMn_T concentrations are minimum values since the sediments were sampled under air.

Silicic acid concentrations increased from seawater levels (~5 µM) to near constant values of ~200 µM in the short cores. They increased again to over 600 µM at 120 cm depth and then dropped to lower levels below 300 cm. Dissolved phosphate showed largely similar trends.

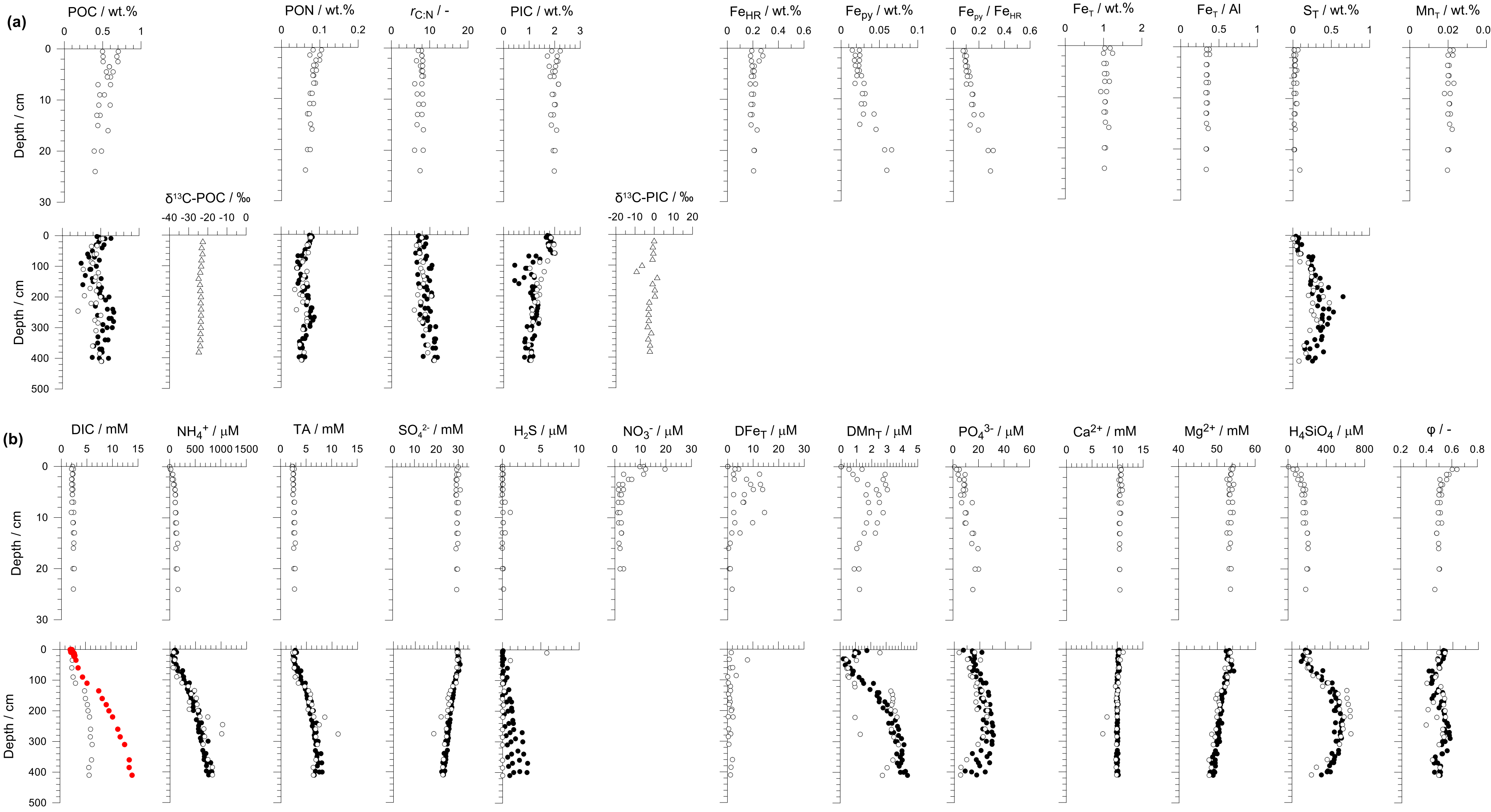
(a)
POC / wt.%
0 0.5 1
PON / wt.%
0 0.1 0.2
$r_{C:N}$ / -
0 10 20
PIC / wt.%
0 1 2 3
Fe_{HR} / wt.%
0 0.2 0.4 0.6
Fe_{py} / wt.%
0 0.05 0.1
Fe_{py} / Fe_{HR}
0 0.2 0.4 0.6
Fe_T / wt.%
0 1 2
Fe_T / Al
0 0.5 1
S_T / wt.%
0 0.5 1
Mn_T / wt.%
0 0.02 0.04
Depth / cm
0 10 20 30
δ^{13}C-POC / ‰
-40 -30 -20 -10 0
δ^{13}C-PIC / ‰
-20 -10 0 10 20
Depth / cm
0 100 200 300 400 500
(b)
DIC / mM
0 5 10 15
NH_4^+ / µM
0 500 1000 1500
TA / mM
0 5 10 15
SO_4^{2-} / mM
0 10 20 30
H_2S / µM
0 5 10
NO_3^- / µM
0 10 20 30
DFe_T / µM
0 10 20 30
DMn_T / µM
0 1 2 3 4 5
PO_4^{3-} / µM
0 20 40 60
Ca^{2+} / mM
0 5 10 15
Mg^{2+} / mM
40 50 60
H_4SiO_4 / µM
0 400 800
φ / -
0.2 0.4 0.6 0.8
Depth / cm
0 10 20 30
Depth / cm
0 100 200 300 400 500

Fig. 3. Sediment geochemistry at the Goldeneye site for (a) solids, and (b) solutes and porosity. The upper panels in (a) and (b) show data from the short cores (upper 30 cm) whereas the lower panels correspond to the long cores (upper 400 cm). Open and filled symbols correspond to data from POS518 and POS534, respectively. Key: POC: particulate organic carbon; δ^{13}C-POC: isotopic composition of POC; PON: particulate organic nitrogen: $r_{C:N}$: organic carbon-to-nitrogen ratio; PIC: particulate inorganic carbon; δ^{13}C-PIC: isotopic composition of PIC; Fe_{HR}: highly reactive iron; FeS_2: pyrite; Fe_{py}/Fe_{HR}: pyrite-to-highly reactive iron ratio; Fe_T: total iron; Fe_T/Al: total iron-to-aluminum ratio; S_T: total sulfur; Mn_T: total manganese; DIC: dissolved inorganic carbon; NH_4^+: total dissolved ammonium; TA: total alkalinity; SO_4^{2-}: sulfate; H_2S: total dissolved hydrogen sulfide; NO_3^-: nitrate; DFe_T; total dissolved iron; DMn_T; total dissolved manganese; PO_4^{2-}: total dissolved phosphate; Ca^{2+}: calcium; Mg^{2+}: magnesium; H_4SiO_4: silicic acid, φ: porosity. The red symbols show DIC concentrations corresponding to a $r_{C:S}$ value of 1.75 and a POC oxidation state of -0.6 (see Discussion).

4.3 Sulfate reduction rates (SRR)

Sulfate reduction rates are shown on a log-log plot in Fig. 4. SRR at the sediment surface were 17.9 ± 5.6 nmol cm^{-3} d^{-1} and remained at similar levels down to 16 cm that could be explained by homogenization of the surface layer by animals. From here, SRR decreased quasi-linearly down to 41 ± 8 pmol cm^{-3} d^{-1} at 100 cm. Below 100 cm, SRR showed no further discernible decrease with depth down to the bottom of the core. The depth-integrated SRR in the surface samples (push core) and deep samples (gravity core) equaled 2.2 and 1.0 mmol m^{-2} d^{-1} of S, respectively, giving a total of 3.2 mmol m^{-2} d^{-1} of S.

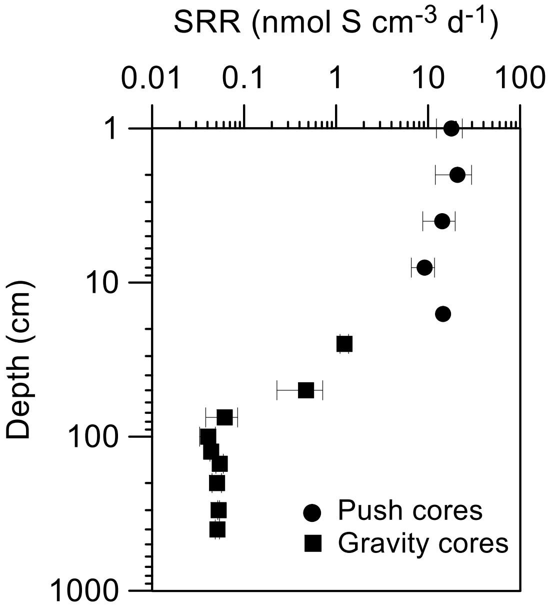

Fig. 4. Sulfate reduction rates (mean ± SD) at Goldeneye on a log-log plot. The mean ± SD SRR from the sample at 16 cm in the push core data was 14.5 ± 18.2 nmol cm^{-3} d^{-1}. The error bars are not shown for this datum since they go below zero.

4.4 Benthic fluxes

Fluxes of solutes determined from the two BIGO deployments are listed in Table 3. TOU_{BC} ranged from 5.2 to 6.7 mmol m^{-2} d^{-1}. Fluxes of NO_3^- were directed out of the sediment to the water column, yet only weakly (-0.07 to -0.10 mmol m^{-2} d^{-1}). NH_4^+ concentrations in the syringe samples were scattered between 2 and 3 µM and a reliable flux could not be determined (not shown). Fluxes of H_4SiO_4 were -0.41 to -0.63 mmol m^{-2} d^{-1} whereas PO_4^{3-} fluxes were -0.03 ± 0.003 mmol m^{-2} d^{-1} on average. N_2 fluxes measured in one chamber during each BIGO deployment were similar and directed from the sediment to the bottom water (-0.20 mmol m^{-2} d^{-1} of N_2).

Table 3. Sediment fluxes of solutes (± SD) across the sediment-water interface measured in situ with benthic chambers (in mmol m^{-2} d^{-1}). Positive fluxes are directed into the sediment and vice versa. (n.d. = not determined).

	NO_3^-	PO_4^{3-}	H_4SiO_4	N_2	TOU_{BC}
3 BIGO1-1 C1	-0.07	-0.033	-0.41	-0.23	5.20
3 BIGO1-1 C2	-0.06	-0.030	-0.51	n.d	6.40
8 BIGO1-2 C1	-0.06	-0.028	-0.62	-0.17	6.70
8 BIGO1-2 C2	-0.10	-0.026	-0.63	n.d	6.40
Mean	-0.07	-0.029	-0.54	-0.20	6.18
SD	0.02	0.003	0.09	0.04	0.58

Total oxygen uptake determined with EC is listed in Table 4. TOU_{EC} ranged from 3.83 ± 1.44 mmol m^{-2} d^{-1} to 10.0 ± 6.85 mmol m^{-2} d^{-1}. At all sites, an increase in oxygen flux into sediments was observed with increasing water velocity. For example, at station 90, TOU_{EC} increased from 4 to 8 mmol m^{-2} d^{-1} as tidally-driven water velocity increased from 5 to 19 cm s^{-1}. A portion of the velocity-dependent contribution may be due to the effect of water velocity on the equilibrium distribution of dissolved oxygen in the lowest ~ 1 m of the water column (Holtappels et al., 2013). However, this effect is small and short-lived relative to the effect that we observed. Measured over sufficient time intervals, transient velocity effects will cancel out. The mean, time-averaged TOU_{EC} was 5.73 ± 2.03 mmol m^{-2} d^{-1} and similar to TOU_{BC}. It is worth noting that at Station 1-4 uptake was the highest during the final two days of the twelve-day experiment (Tukey HSD, $p < 0.05$). Disturbance of the seafloor by ROV operations may have contributed to this.

Table 4. Dissolved O_2 fluxes across the sediment-water interface measured in situ by eddy covariance (in mmol m^{-2} d^{-1}). n refers to the number of half-hour intervals used for flux calculations (due to bad weather, measurement intervals at station 13-1 were only ten minutes long). Standard deviation includes variance that is due to a velocity-dependence of O_2 uptake.

Station	Campaign	n	TOU_{EC}	SD
13-1	POS518	3	5.38	2.08
59	POS527	9	3.83	1.44
76	POS527	29	4.94	2.31
90	POS527	17	5.71	2.65
121	POS527	10	4.28	1.78
1-2	JC180	24	5.95	3.42
1-4	JC180	60	10.0	6.85
Mean			5.73	2.03

4.5 Bioirrigation, bioturbation and sedimentation rates

At the end of the experimental incubations, Br^- had infiltrated 8 – 10 cm into the sediment compared to a theoretical 5 cm if diffusion were the only transport pathway for solutes (Fig. 5). This difference is assumed to be caused by enhanced solute pumping by animals. Simulated bioirrigation coefficients (α_1) required to fit the data from the different cores were similar at 61 ± 11 yr^{-1}, 86 ± 20 yr^{-1}, and 65 ± 12 yr^{-1}, respectively. The parameters controlling the irrigation depth (α_2) were also similar at 4.5 ± 0.5 cm, 3.3 ± 0.5 cm, and 3.6 ± 0.4 cm, respectively. The mean of these parameters was used to plot the depth-dependent bioirrigation coefficient in Fig. 5e. It shows that solute pumping through animal burrows affected the upper 8 cm of the sediment. This agrees well with the depth of burrow traces observed through the Perspex liners of the multiple-cores, presumably due to the polychaete *Paramphinome jeffreysii* (Mesher et al., 2020).

The importance of bioirrigation as a pathway for solute transport relative to molecular diffusion can be illustrated by comparing the total flux using the benthic chambers with the diffusive flux at the sediment-water interface. Taking silicic acid as an example, the diffusive flux at the sediment surface, J_{Si}, can be calculated using Fick's Law:

$$J_{Si} = -\varphi D_{Si} \frac{\partial[Si]}{\partial x}\bigg|_{x=0} \qquad (6)$$

where $\partial[Si]/\partial x$ denotes the silicic acid concentration gradient at the sediment surface (x=0), φ is the surface porosity (0.62), and D_{Si} is the bulk molecular diffusion coefficient of silicic acid in the sediment (Table 5). $\partial[Si]/\partial x$ is calculated as the difference between the bottom water silicic acid concentration (Si_{olw} = 6 µM) and that in the uppermost sediment layer at 0.5 cm in the undisturbed multiple-core data. It equals 95 to 170 nmol cm^{-3} cm^{-1} for MUC1 and 2, respectively. J_{Si} is then -0.16 to -0.32 mmol m^{-2} d^{-1}, which compares to -0.54 mmol m^{-2} d^{-1}

from the benthic chambers (Table 3). The bioirrigation flux is, by difference, -0.22 to -0.38 mmol m^{-2} d^{-1}.

The contribution of bioirrigation can also be calculated by integrating the bioirrigation term $\alpha_{bi}\varphi(\mathrm{Si}_{\mathrm{olw}} - \mathrm{Si}^{-})$ over depth (c.f. Eq. (1)). This equals -0.33 mmol m^{-2} d^{-1} (MUC1) and -0.49 mmol m^{-2} d^{-1} (MUC2), which is in good agreement with the previous estimate. It can be concluded that bioirrigation markedly intensifies benthic-pelagic coupling and recycling of nutrients at Goldeneye.

$^{210}\mathrm{Pb}_{\mathrm{xs}}$ was scattered, but showed a gradual decrease of ca. 0.02 Bq g^{-1} in the upper 5 to 10 cm, and then dropped toward zero by 20 cm (Fig. 6). The model simulation to the data was achieved by fixing the bioturbation halving-depth (x_B) to 5 cm, thus assuming a mixed depth of ~10 cm. This depth was based on the bioirrigation experiment results and observed animal burrows. The simulated best-fit surface mixing coefficient (D_{B0}) was 12.1 ± 1.4 cm^2 yr^{-1}. Below the mixed layer, the decrease in $^{210}\mathrm{Pb}_{\mathrm{xs}}$ was captured using a sediment accumulation rate (ω_{acc}) of 0.11 ± 0.01 cm yr^{-1}. Using the porosity in the short cores at 10 cm (0.5) and a dry sediment density (ρ) of 2.5 g cm^{-3}, the mass accumulation rate (MAR) of bulk sediment at Goldeneye is equal to $\omega_{\mathrm{acc}} \times \rho \times (1 - \varphi) = 0.11 \times 2.5 \times 0.5 = 0.14$ g cm^{-2} yr^{-1}.

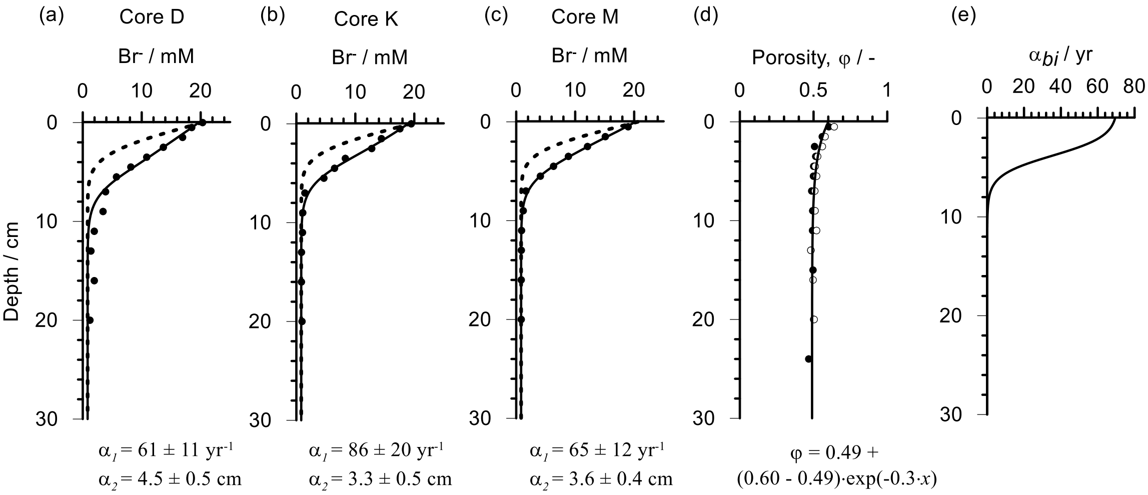

Fig. 5. Sediment depth profiles of measured (symbols) and modeled (curves) bromide (Br$^-$) concentrations at the end of the whole core incubations in cores (a) D, (b) K, and (c) M. The dashed lines indicate the transport of Br$^-$ as expected by molecular diffusion only. The coefficients α_1 (yr^{-1}) and α_2 (cm) are provided. (d) The measured porosity and best-fit curve used in the numerical simulation. (e) The change in the bioirrigation coefficient with depth calculated with Eq. (3) and the mean α_1 and α_2 values.

Table 5. Bulk diffusion coefficients in sediments at Goldeneye.

Constituent (unit) [a]	Value
Sulfate, $D_{\mathrm{SO_4^{2-}}}$ (cm^2 yr^{-1})	209
Dissolved inorganic carbon, D_{DIC} (cm^2 yr^{-1}) [b]	227
Total alkalinity, D_{TA} (cm^2 yr^{-1}) [c]	227
Ammonium, $D_{\mathrm{NH_4^+}}$ (cm^2 yr^{-1})	396
Silicic acid, D_{Si} (cm^2 yr^{-1})	205
Magnesium, $D_{\mathrm{Mg^{2+}}}$ (cm^2 yr^{-1})	142

[a] Diffusion coefficients were calculated for the local salinity (35) and temperature (9.5 °C) (Boudreau, 1997; Schulz, 2000). They can be corrected for sediment tortuosity by dividing by $1-\ln(\varphi^2)$, where φ is the sediment porosity.

[b] Assumed to be equal to the diffusion coefficient of bicarbonate. HCO_3^- (Emerson et al., 1980; Burdige and Komada, 2011).

[c] Assumed to be equal to D_{DIC} (Emerson et al., 1980).

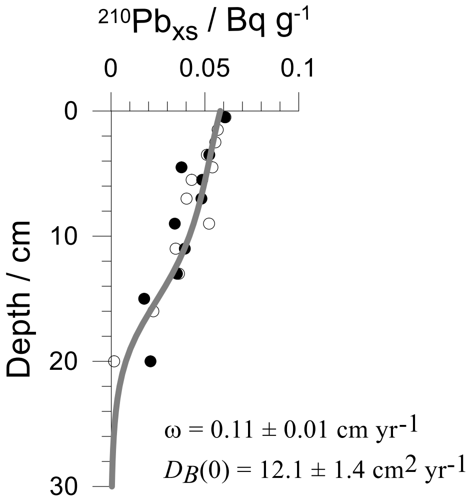

Fig. 6. Measured (symbols) and modeled (curve) $^{210}Pb_{xs}$. Model-derived sediment accumulation rate and bioturbation coefficient are shown. Different symbols correspond to replicate cores (MUC 1 and MUC 2).

5. Discussion

5.1 POC degradation and burial in Goldeneye sediments

Sediments in the North Sea generally have a high sand content and are depleted in organic carbon compared to fine-grained muds (Diesing et al., 2017). The mean POC content in the short cores sampled at Goldeneye (~0.53 %) is similar to the mean value reported for the NW European continental shelf (0.46 %, Diesing et al., 2017). The organic matter is also depleted in PON ($r_{C:N}$ ~8.5) compared to phytoplankton with Redfield stoichiometry ($r_{C:N}$ ~6.6). The mean δ^{13}C-POC of -23.7 ‰, together with $r_{C:N}$ values < 10, demonstrate that organic matter at Goldeneye has a predominantly marine provenance (Meyers, 1994; Zeebe and Wolf-Gladrow, 2001).

Following deposition on the seafloor, POC becomes entrained in the sediment pile by burial and bioturbation. The easily degradable organic components are simultaneously mineralized back to inorganic solutes (DIC, NH_4^+, PO_4^{3-}, H_4SiO_4), leading to a decrease in POC content over time (Berner, 1980). This process is evident by the increase in concentrations of these solutes with depth in the sediment, as well as total alkalinity, and by the decrease in POC in the upper meter (Fig. 3). However, there are indications that POC degradation has changed over time. Following the initial decrease in POC down to 100 cm, the POC (and PON) content begins to increase again with depth. According to the sedimentation rate of 0.11 cm yr^{-1}, the age of the 100 cm horizon is ~900 yr. The increase could be caused by the observed transition to more fine-grained material at this depth because POC content is closely linked to mineral grain size (Mayer, 1994). However, we observed no correlation between grain size and POC content at this site. The POC increase could also be driven by a change in bulk sediment accumulation rate and/or POC rain rate to the seafloor. Better age control of these deeper sediment layers is required for a more definitive explanation. Non-steady state conditions are also inferred from the near constant SRR below 100 cm following the steep decrease from the sediment surface down to that depth (Fig. 4). For steady-state sediment accumulation, SRR typically displays a quasi-linear decrease over depth on a double-log plot such as that presented in Fig. 4 (Jørgensen, 1978; Jørgensen and Parkes, 2010; Holmkvist et al., 2011; Flury et al., 2016; Dale et al., 2019). This reflects the availability of degradable organic matter that decreases by many orders-of-magnitude with depth or, more correctly, with age (Middelburg, 1989).

In sediments underlying O_2-saturated bottom waters, POC remineralization (R_{POC}) can be estimated from the TOU and $r_{C:N}$:

$$R_{POC}=\frac{TOU}{1+2/r_{C:N}} \tag{7}$$

Taking the mean of the TOU_{BC} and TOU_{EC} (6.0 mmol m^{-2} d^{-1}) and the $r_{C:N}$ of 8.5, R_{POC} can be calculated as 4.8 mmol m^{-2} d^{-1}, which is within the range expected for the North Sea (Luff and Moll, 2004). The POC burial flux, derived from the POC content of 0.51 % at 10 cm (i.e. the globally averaged mixed layer depth (Boudreau, 1997)) and the sediment mass accumulation (MAR, 0.14 g cm^{-2} yr^{-1}), is 1.6 mmol m^{-2} d^{-1}.

The data now allow for an estimation of the fraction of POC that escapes remineralization to DIC and gets buried below the mixed layer, that is, the carbon burial efficiency (CBE). The CBE is equal to 100 % × POC burial / POC rain rate to the seafloor, where the rain rate can be approximated as the sum of POC burial and R_{POC}, assuming steady-state conditions. The POC rain rate to the seafloor is thus 6.4 mmol m^{-2} d^{-1}, giving a CBE of 25 %. This is within the range of 15 – 60 % expected for the sediment MAR at Goldeneye (Canfield, 1993).

There is inevitably some uncertainty in these fluxes, not least because of the abrupt change in POC degradation with sediment depth at 100 cm depth. However, because most organic matter in marine sediments is degraded in the upper 10 - 20 cm (Flury et al., 2016), the largest uncertainty comes from the measured TOU and the recent sediment accumulation rate constrained from $^{210}Pb_{xs}$. The good agreement between TOU_{BC} and TOU_{EC} suggests that the oxygen fluxes are reliable. The data are also of similar magnitude to TOU measured in the northern North Sea from core incubations (Brenner et al., 2016) and benthic chambers (McGinnis et al., 2014). The variability in the EC measurements, which were made on several occasions at different times of the year, is not enough to suggest that the TOU fluxes were biased toward periods of low or high benthic activity.

Sediment accumulation rates across the wider region range from 0.05 to 0.35 cm yr^{-1} and bracket the value of 0.11 cm yr^{-1} reported here (de Haas et al., 1997). The determination of sediment accumulation rates from $^{210}Pb_{xs}$ data depends on being able to specify the mixing depth (x_B). A mixing depth of ~10 cm was assumed based on the bioirrigation experiment results and observed animal burrows. Seafloor biota at Goldeneye is dominated by shallow-dwelling polychaetes (Mesher et al., 2020). Yet, deeper sediment mixing by other macrofauna cannot be excluded. Furthermore, trawling activities that are widespread in the area can mix the top 15 – 20 cm of sediment, depending on the sediment type and trawling gear (Eigaard et al., 2016). Analogous to bioturbation, episodic trawling would enhance the penetration of particles, including ^{210}Pb, to deeper sediment layers, giving the impression of elevated accumulation rates (and CBE) when $^{210}Pb_{xs}$ is interpreted using a steady-state model. ^{137}Cs (half-life 30 yr) distributions were consistently low in the upper 20 cm (1.8 ± 0.5 Bq kg^{-1}, not shown) with no obvious trace of the Chernobyl accident (1983) or input from nuclear weapons testing (1954 - 1963). This could be interpreted as a mixing depth considerably larger than 10 cm. Additional analysis of shorter-lived tracers such as ^{7}Be (half-life 53 d), ^{234}Th (half-life 24 d) or photosynthetic pigments (e.g. chlorophyll a) would be useful to make further inferences on deep sediment mixing. On balance, it is our opinion that the MAR derived here may be too high and should be interpreted cautiously.

5.2 Biogeochemical zonation prior to CO_2 injection

In marine sediments, POC is respired by microorganisms using a series of electron acceptors that are used sequentially according to the energy released per mole of POC oxidized. This results in a predictable vertical stratification of main respiratory pathways (Froelich et al., 1979; Megonigal et al., 2004). In the surface layer where O_2 is present, aerobic microorganisms dominate. Microsensor profiles of dissolved O_2 made in situ at Goldeneye revealed an aerobic layer < 1 cm thick (de Beer et al., this issue). In the nearby Tommeliten area, O_2 penetration depths ranged from 0.2 to 0.8 cm and were dependent on the tidal current velocity (McGinnis et al., 2014).

The aerobic layer overlies a nitrogenous layer where NH_4^+ is oxidized to NO_3^- and, in turn, NO_3^- is transformed to N_2 by denitrification and/or anammox. At Goldeneye, the decrease in NO_3^- shows that this layer extends to ~4 cm depth. A fraction of porewater NO_3^- must be derived from the nitrification of PON-derived NH_4^+ because the benthic NO_3^- flux was directed out of the sediment (-0.073 mmol m^{-2} d^{-1}). This is also inferred from the positive concentration gradient of NO_3^- at the sediment surface (Fig. 3). The N_2 efflux indicates that 0.4 mmol m^{-2} d^{-1} of fixed N is consumed by denitrification and anammox. We cannot currently estimate the relative importance of these pathways, but we can use the data to calculate the expected NH_4^+ flux from the sediment assuming fixed N loss by denitrification. If TOU is a proxy for the depth-integrated rate of POC oxidation, NH_4^+ should be produced from the breakdown of organic matter at a rate of TOU/$r_{C:N}$. This is equal to 0.69 mmol m^{-2} d^{-1} using the numbers given above to calculate R_{POC}. Subtracting the N_2 and NO_3^- fluxes from this number gives a net flux of NH_4^+ of -0.22 mmol m^{-2} d^{-1}. This would not be detectable in the benthic chambers for the deployment times used in this study (36 h) because NH_4^+ concentrations would increase by only ~2 µM. This increase is within the scatter of the measured data (not shown). The NH_4^+ flux would be even lower if anammox contributes significantly to the N_2 flux. Overall, denitrification accounts for up to ~4 % of POC respiration at Goldeneye, which is a typical value for marine sediments (Thullner et al., 2009).

The nitrogenous layer apparently overlaps a manganous and ferruginous layer with measurable DMn_T (<3 µM) and DFe_T (<12 µM) concentrations down to 15 cm. Metal oxides generally account for a minor fraction of POC respiration in coastal sediments, although there are notable exceptions where large amounts of terrigenous material are deposited on the seafloor (e.g. Canfield et al., 1993) or in sediments that are intensely bioturbated (Aller, 1990). The low concentrations suggest a negligible contribution of Fe(III) and Mn(IV) to POC respiration, although oxidation of Fe^{2+} and Mn^{2+} during sample processing could skew the observations. Fe^{2+} and Mn^{2+} levels in sediments sampled under an O_2-free atmosphere were up to 56 µM and 7 µM, respectively (Lichtschlag et al., this issue). Fe^{2+} and Mn^{2+} levels can also be kept low by pumping of oxygenated water into the sediment through animal burrows or by tidal pumping in permeable sediments (Marinelli et al., 1998). The absence of significant DIC and TA accumulation in the short cores (tracers of organic matter degradation) is indicative of solute flushing by bioirrigation (Fig. 5).

The majority of the sediment column from ~30 cm depth to the bottom of the gravity cores is weakly sulfidic and hence classified as sulfate reducing. Sulfate reduction was detectable throughout the whole sediment with highest rates in the ferruginous and nitrogenous zones (Fig. 4). The presence of FeS_2 at the surface implies that sulfate reduction is active there even though porewaters are depleted in H_2S (Thamdrup et al., 1994). Dissolved H_2S can be completely precipitated as iron sulfide phases if dissolved Fe^{2+} released from the reduction of iron (oxyhydr)oxides exceeds H_2S production by sulfate reduction (Jørgensen et al., 2019). At Goldeneye, this process is probably enhanced by bioturbation and the mixing of iron (oxyhydr)oxide particles into H_2S-bearing sediments. Sediment mixing provides a mechanism by which iron can be repeatedly shuttled through oxidized and reduced phases, helping to maintain low H_2S levels before permanent S burial as iron sulfides or organic S (Aller, 1990; Van Cappellen and Wang, 1996).

By extrapolating the SO_4^{2-} concentration gradient downwards, the depth where SO_4^{2-} is predicted to become exhausted and where methanogenesis begins is around 20 m, which is well below the base of the Witch Ground Formation (4 – 7 m) (Connelly, 2019). It is therefore unlikely that microbial breakdown of organic matter in the Witch Ground Formation provides a significant source of methane (see also Böttner et al., 2019). This agrees with hydroacoustic profiling that showed no seismic blanking in the Witch Ground sediments caused by free gas bubbles (Böttner et al., 2019; Connelly, 2019).

5.3 Stoichiometric diagnostic indicators of organic matter remineralization

Aside from a qualitative description of Goldeneye sediments, a biogeochemical baseline should also ideally include quantitative properties that can be incorporated into a monitoring program for CO_2 leakage. This could be ratios of benthic DIC fluxes relative to other species such as nutrients or O_2. Yet, nutrient, DIC and O_2 fluxes typically show high spatial and temporal variability within an individual system (Andersson, 2007), requiring CO_2 leakage fluxes at the seafloor to be well above the background noise to be detectable (see Blackford et al., 2015). In the following discussion, we focus instead on stoichiometric indictors that describe quantitatively the co-distribution of solutes in the sediment porewater prior to the controlled CO_2 release experiment. We do this for the sediment layers where organic matter is being degraded in the sulfate reduction zone. These sediments are likely to be unaffected by seasonal changes in particle rain rates to the sea floor and by trawling activities.

In general, for organic matter with a chemical composition of $C_aH_bN_cO_dP_e$, the reaction stoichiometry that defines sulfate reduction is the following (LaRowe and Van Cappellen, 2011):

$$\mathrm{C}_a\mathrm{H}_b\mathrm{N}_c\mathrm{O}_d\mathrm{P}_e + \frac{(4-ox)a}{8}\mathrm{SO}_4^{2-} \rightarrow a\mathrm{HCO}_3^- + c\mathrm{NH}_4^+ + e\mathrm{HPO}_4^{2-} + \frac{(4-ox)a}{8}\mathrm{HS}^- + \left(-\frac{(4-ox)a}{8} + a - c + 2e\right)\mathrm{H}^+ + \left(\frac{(4-ox)a}{2} - 3a + d - 4e\right)\mathrm{H}_2\mathrm{O} \qquad (8)$$

where *ox* is the oxidation state of the organic carbon undergoing remineralization. For an uncharged molecule, *ox* is formerly defined as (LaRowe and Van Cappellen, 2011):

$$ox = 4 - \frac{4a+b-3c-2d+5e}{a} \qquad (9)$$

In marine sediments, *ox* ranges from -0.5 to -0.7 (Burdige, 2006). Natural POC is thus more reduced than the zero oxidation state implied by Redfield stoichiometry ($C_{106}H_{263}O_{110}N_{16}P$).

From Eq. (8), the moles of NH_4^+ produced per mole of SO_4^{2-} reduced, $r_{\mathrm{N:S}}$, can be defined as:

$$r_{\mathrm{N:S}} = \frac{8\cdot {}^{c}/_{a}}{(4-ox)} = \frac{8}{(4-ox)\, r_{\mathrm{C:N}}} \qquad (10)$$

If solute transport by burial is negligible compared to molecular diffusion, which is the case for most slowly accumulating sediments, $r_{\mathrm{N:S}}$ can be estimated from a property-property plot of porewater NH_4^+ versus SO_4^{2-} concentrations (Burdige, 2006; Burdige and Komada, 2013). The left hand-hand side of the following equation is the slope of the linear regression of the data shown in Fig. 7:

$$\frac{d\mathrm{NH_4^+}}{d\mathrm{SO_4^{2-}}} = -r_{\mathrm{N:S}} \frac{D_{\mathrm{SO_4^{2-}}}}{D_{\mathrm{NH_4^+}}} \tag{11}$$

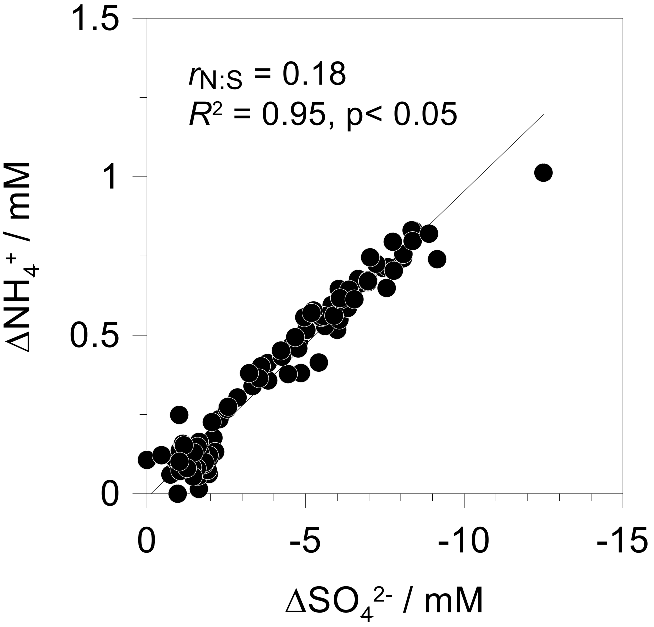

Fig. 7. NH_4^+-SO_4^{2-} property-property plot at Goldeneye. The slope of the correlation (dNH_4^+/dSO_4^{2-}) is used to calculate $r_{\mathrm{N:S}}$ (see text). The capital delta (Δ) indicates that the concentrations are relative to bottom water values.

Correcting the regression slope for the ratio of the bulk molecular diffusion coefficients (Table 5) allows $r_{\mathrm{N:S}}$ = 0.18 to be derived. It is lower than the value of 0.30 expected for Redfield POC, which agrees with the previous discussion that the organic matter is depleted in N. The factor $r_{\mathrm{N:S}}$ can be used as a stoichiometric indicator for the baseline distributions of NH_4^+ and SO_4^{2-} in undisturbed porewaters at Goldeneye. Subsequently, from Eq. (10), we can calculate a value of *ox* = -1.12 using the previously derived $r_{\mathrm{C:N}}$ (8.5). It suggests that organic matter being remineralized at Goldeneye is more reduced than the organic matter in the studies compiled by Burdige (2006).

The impact of CO_2 leakage on NH_4^+ and SO_4^{2-} levels is unknown, but it is expected to be minor compared to changes in DIC and TA due to CO_2 dissolution and to CO_2–driven dissolution of carbonate and aluminosilicate minerals (Lichtschlag et al., 2015). Arguably a more sensitive indicator for CO_2 leakage in sulfate reducing sediments, therefore, is the moles of POC oxidized to DIC per mole of SO_4^{2-} reduced, $r_{\mathrm{C:S}}$ (Burdige, 2006; Jørgensen and Parkes, 2010; Burdige and Komada, 2011; Scholz et al., 2013). We calculated $r_{\mathrm{C:S}}$ from a property-property plot of porewater DIC versus SO_4^{2-} concentrations analogous to $r_{\mathrm{N:S}}$ (not shown). However, the derived $r_{\mathrm{C:S}}$ value (0.65) was much lower than that expected for natural marine organic matter (~1.75). Furthermore, a $r_{\mathrm{C:S}}$ of 0.65 is clearly spurious since the minimum possible value is equal to 1, corresponding to the oxidation of carbon with a -4 oxidation state (i.e. the anaerobic oxidation of CH_4 by SO_4^{2-}). The discrepancy could be resolved if the precipitation of carbonate minerals contributes to a lowering of in situ DIC levels in the porewater. In that case, the true $r_{\mathrm{C:S}}$ will be higher than 0.65 (Berelson et al., 2005). Yet, the negligible decrease in Ca^{2+} concentrations with sediment depth implies that the precipitation of authigenic calcium carbonate phases has a minor impact on DIC levels (Fig. 3). Instead, we suspect that loss of dissolved CO_2 during core processing and sample handling may have resulted in low DIC values. By increasing the measured DIC concentration in a stepwise manner with sediment depth, we observed that DIC would need to be a factor of ~1.5 to 2.5 higher in order for the slope of the regression to be consistent with a $r_{\mathrm{C:S}}$ of 1.75 (Fig. 3, red symbols). A more general understanding of the extent of CO_2 degassing from sediment porewaters during core extraction and sample handling warrants further study. We conclude that $r_{\mathrm{C:S}}$ might not be a robust indicator for detecting CO_2 leakage because of potential degassing problems following our sediment processing protocols.

Since TA is not affected by degassing artifacts, the change in TA per mole of SO_4^{2-} reduced, $r_{\mathrm{TA:S}}$, holds more promise as a diagnostic indicator for monitoring CO_2 leakage than $r_{\mathrm{C:S}}$. $r_{\mathrm{TA:S}}$ can be derived from a slope of TA versus SO_4^{2-} concentrations (Fig. 8a):

$$\frac{d\mathrm{TA}}{d\mathrm{SO}_4^{2-}} = -r_{\mathrm{TA:S}}\frac{D_{\mathrm{SO}_4^{2-}}}{D_{\mathrm{TA}}} \qquad (12)$$

Correcting the slope for the diffusion coefficients gives $r_{\mathrm{TA:S}} = 0.79$. There is some uncertainty in this result because D_{TA} is approximated as the diffusion coefficient for HCO_3^- (Table 5). In reality, the porewater composition of proton acceptors (i.e. HCO_3^-, CO_3^{2-}, HS^- …), and hence D_{TA}, very likely changes with depth in the sediment.

As a check on the $r_{\mathrm{TA:S}}$ value, it can be calculated from the reaction stoichiometry in Eq. (8):

$$r_{\mathrm{TA:S}} = \frac{2(4-ox)+\frac{8}{r_{\mathrm{C:N}}}-\frac{8e}{\mathrm{a}}}{(4-ox)} \qquad (13)$$

where $a = 106$, $e = 1$ and $r_{\mathrm{C:N}}$ is 8.5. Inserting the previous ox value of -1.12 into Eq. (13) gives $r_{\mathrm{TA:S}}$ of ~2.17; much higher than derived from Eq. (12). In fact, a $r_{\mathrm{TA:S}}$ value of 0.79 implies an impossible organic carbon oxidation state of +4.7.

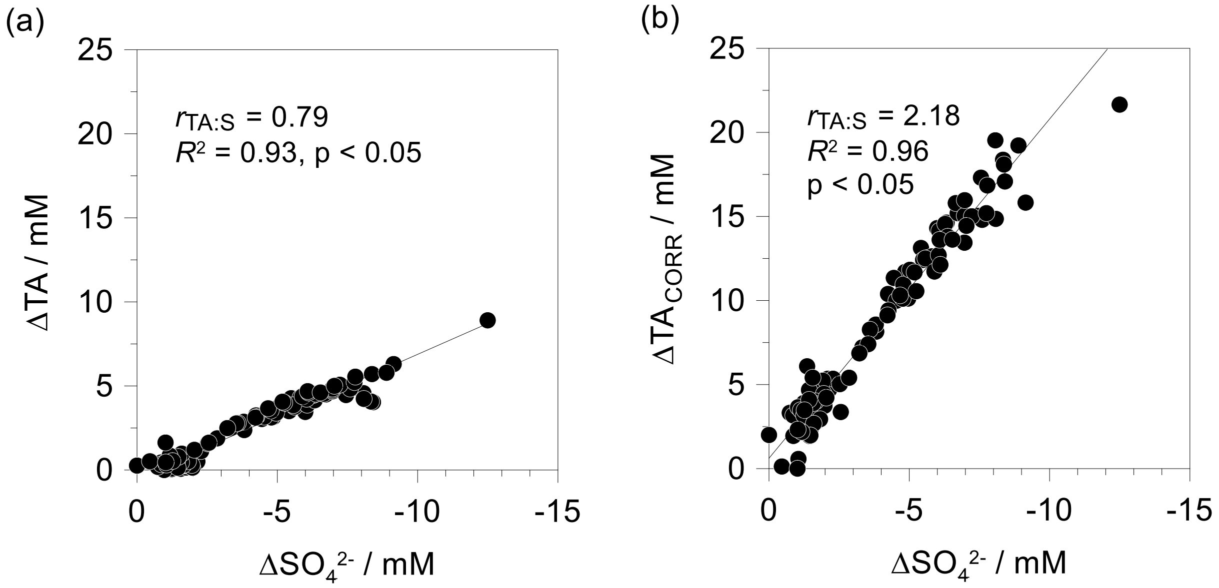

Fig. 8. TA-SO_4^{2-} property-property plots at Goldeneye (a) with measured TA concentrations and (b) with TA concentrations corrected for alkalinity loss by reverse weathering as described in Eq. (15). The capital delta (Δ) indicates that the concentrations are relative to bottom water values.

There is no reason to suspect that the derived $r_{TA:S}$ of 0.79 is a spurious number, and consequently it can be proposed as a stoichiometric indicator for TA and SO_4^{2-} concentrations in the natural setting at Goldeneye. Rather, a more thorough accounting of TA sinks might explain the low value. Although our results suggest that whilst authigenic carbonate formation makes an insignificant contribution to TA consumption, the formation of cation-rich authigenic clay minerals from weathered aluminosilicates might be important. Otherwise known as reverse weathering, this ubiquitous process in marine sediments can be described in general terms as (MacKenzie and Garrels, 1966; Michalopoulos and Aller, 1995; Wallmann et al., 2008):

Biogenic opal + metal hydroxides + dissolved cations + HCO_3^- → clay minerals + CO_2 (14)

Dissolved cations bound into the authigenic silicate phase include Mg^{2+}, Na^+, and K^+. Opal was not measured, but the high silicic acid levels are evidence of its presence (Fig. 3). We suggest that reverse weathering is responsible for the notable decrease in Mg^{2+} by 6 – 7 mM in the upper 400 cm (Fig. 3). To interpret this decrease in the context of decreasing Cl^- concentrations (Fig. 9a), the Mg^{2+} data were normalized to Cl^-. The normalized Mg^{2+} concentrations show a negative and significant decrease with depth (p<0.05, Fig. 9b). Na^+ also shows a significant decrease, whereas K^+ shows a much weaker positive slope, that is, a slight source of K^+.

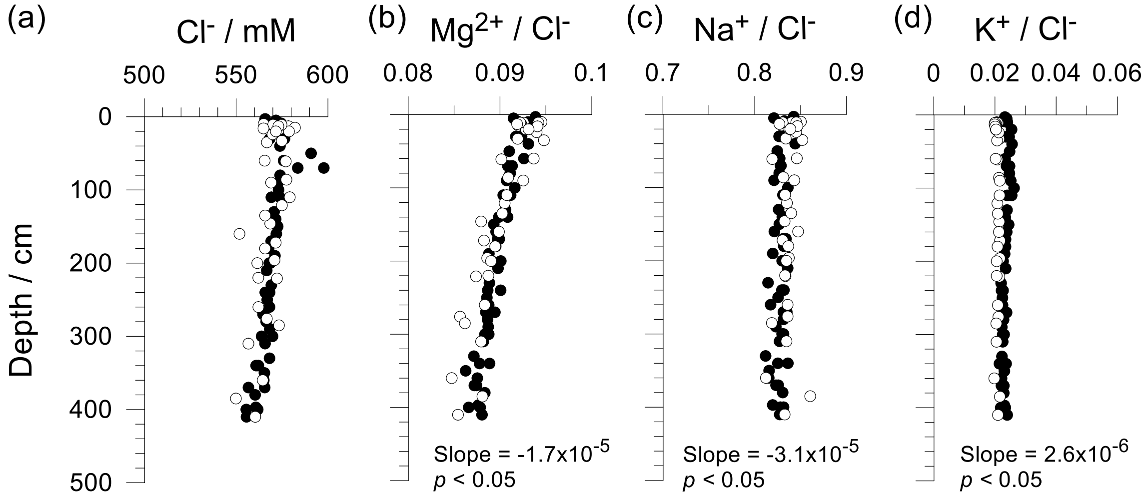

Fig. 9. Concentrations of (a) Cl- and (b) – (d) Cl^--normalized concentrations of Mg^{2+}, Na^+, and K^+. See Fig. 3 for further details. The slope and significance level of the linear regressions through the normalized data are shown. The MUC data from the surface mixed layer (≤ 10 cm) were not used in the regressions.

With this new information, the TA data can be corrected for authigenic clay formation by adding the difference between the cation concentrations in seawater measured at Goldeneye and those measured at each depth in the sediment:

$$\mathrm{TA_{corr}} = \mathrm{TA} + 2\,(\mathrm{Mg^{2+}_{SW}} - \mathrm{Mg^{2+}}) + (\mathrm{K^{+}_{SW}} - \mathrm{K^{+}}) \qquad (15)$$

where seawater concentrations of Mg^{2+} (Mg^{2+}_{SW}) and K^+ (K^+_{SW}) measured in the bottom water are 54 mM and 10.1 mM, respectively. The factor ‘2’ in Eq. (15) accounts for the fact that loss of one Mg^{2+} ion decreases TA by two equivalents. TA data were not adjusted for Na^+ because the correction term was smaller than the analytical precision of the Na^+ measurement (2 %) for two-thirds of the data set. Replotting the data with the corrected TA data (Fig. 8b) now gives $r_{\mathrm{TA:S}} = 2.18$, which is very similar to the value derived from the NH_4^+ and SO_4^{2-} concentrations (2.17).

The rate of reverse weathering can be estimated as the downward diffusive flux of Mg^{2+} using Fick’s law, $J_{Mg^{2+}}$:

$$J_{Mg^{2+}} = -\varphi D_{Mg^{2+}} \frac{\partial[\mathrm{Mg^{2+}}]}{\partial x} \qquad (16)$$

where $\partial[Mg^{2+}]/\partial x$ denotes the dissolved Mg^{2+} concentration gradient (-0.013 μmol cm^{-3} cm^{-1}), φ is the mean porosity of the sediment layer where $\partial[Mg^{2+}]/\partial x$ is calculated (0.5), and $D_{Mg^{2+}}$ is the bulk molecular diffusion coefficient of Mg^{2+} in the sediment (Table 5). The potential loss of TA into authigenic clay minerals is then 0.014 mmol m^{-2} d^{-1}, which is less than 1 % of the TOU. Apparently, then, very low rates of reverse weathering can have a large effect on $r_{\mathrm{TA:S}}$. This result is encouraging because it implies that low rates of alkalinity generation from mineral dissolution in the event of CO_2 leakage ought to be detectable against the unperturbed background signal.

5.4 Summary and recommendations

A comprehensive biogeochemical analysis of the upper 4 – 5 m of Witch Ground Formation sediments at Goldeneye is described, including the analysis of porewater and solid phase chemical species in addition to sediment mixing rates by animals. It provides a baseline for interpreting the results of the shallow CO_2 release experiment that took place in May 2019 (Flohr et al., this issue).

Release of CO_2 to sediment porewaters, either experimentally or accidentally, is expected to increase the concentrations of DIC and TA as a result of CO_2-mineral interactions. The distribution of DIC, TA and other solutes in porewaters has been described quantitatively at the Goldeneye site using stoichiometric relationships between TA, NH_4^+ and SO_4^{2-} ($r_{\mathrm{N:S}}$, $r_{\mathrm{TA:S}}$). They could be extended to include other components such as silicic acid and major ions. In the event of CO_2 leakage, TA concentrations ought to display more deviation from baseline values than NH_4^+ and SO_4^{2-}, and an increase in $r_{\mathrm{TA:S}}$ relative to $r_{\mathrm{N:S}}$ is expected. Furthermore, CO_2–induced dissolution of clay minerals may lead to an increase in cation concentrations above background levels and alter the reverse weathering indicators observed at Goldeneye (e.g. Mg^{2+}/Cl^-). This approach requires long sediment cores (e.g. gravity cores) because changes in chemical gradients of solutes caused by CO_2 leakage will be more reliably detectable over large depth scales. Detection of changes in chemical gradients in short cores will be confounded by seasonality in particle rain rates to the seafloor and non-local mixing caused by the movement of animals through the sediment (bioirrigation and bioturbation). Clearly, a sufficient number of replicate cores are required to iron-out local anomalies due to unusual fluid migration pathways in and around pockmarks as well as local sediment heterogeneity.

The use of DIC in porewater stoichiometry models is subject to greater uncertainty due to degassing of CO_2 during sediment sampling and handling. The extent of degassing is currently hard to quantify. Degassing of CO_2 may have contributed to the low measured DIC levels in the sediments investigated here, and a top priority for future work would be to obtain uncompromised pore water DIC values in the monitoring of CCS sites. Degassing problems are largely avoidable if CO_2 leakage detection is based on DIC fluxes across the sediment surface using discrete water samples collected using benthic chambers. However, this requires an understanding of the magnitude of long- (e.g. seasonal) and short-term (e.g. tidal) fluctuations in benthic organic carbon remineralization rates. These fluctuations tend to be high in dynamic coastal systems like the North Sea, potentially leading to false positive and negative signals in field data. Furthermore, CO_2 leakage in benthic chambers must be detectable against the large background seawater DIC pool. Stoichiometric relationships of porewater solutes are arguably more sensitive to CO_2 leakage because they describe the distribution of porewater constituents over the whole sediment profile.

Acknowledgements

The authors would like to thank the captains and crews and RV Poseidon and James Cook for their excellent support during the research expeditions. Biogeochemical analyses were performed by A. Bleyer, B. Domeyer, R. Surberg, A. Bodenbinder and K. Peel and deployment of sediment corers and landers was done by A. Petersen, M. Türk, A. Beck, C. Utecht, S. Cherednichenko and F. Evers. We also thank M. Esposito for assistance on cruises POS527 and POS534, as well as D. Jasinski, M. Martinez Cabanas, and S. Rakshit for assistance with on board sampling and analysis. Sediment data presented in this study are stored on the PANGAEA World Data Center (https://www.pangaea.de/). The eddy covariance data are available from the co-author (DK) upon request. This research received funding from the European Union's Horizon 2020 research and innovation programme under grant agreement No. 654462 (STEMM-CCS). It was also supported by the Max Planck Society. We thank the Associate Editor Charles Jenkins for handling the manuscript.

References

Acatech., 2018. CCU und CCS –Bausteine für den Klimaschutz in der Industrie, Herbert Utz, Verlag München, 76 pp.

Achterberg, E. P. and Esposito, M., 2018. *RV POSEIDON Fahrtbericht / Cruise Report POS527 - Baseline Study for the Environmental Monitoring of Subseafloor CO_2 Storage Operations, Kiel – Kiel (Germany), 15.8. - 3.9.2018.* GEOMAR Report, N. Ser. 045 . GEOMAR Helmholtz-Zentrum für Ozeanforschung, Kiel, Germany, IV, 90 pp. DOI 10.3289/geomar_rep_ns_45_2018.

Aller R. C., 1990. Bioturbation and manganese cycling in hemipelagic sediments. *Philos. Trans. R. Soc. A* 331, 51–68.

Alperin M. J., Suayah I. B., Benninger L. K. and Martens C. S., 2002. Modern organic carbon burial fluxes, recent sedimentation rates, and particle mixing rates from the upper continental slope near Cape Hatteras, North Carolina (USA). *Deep-Sea Res. II* 49, 4645–4665.

Andersson, J. H., 2007. *Respiration in ocean margin sediments*. PhD thesis, Utrecht University, Geologica Ultraiectina, 283 ISBN: 978-90-5744-148-6.

Berelson W. M., Prokopenko M., Sansone F. J., Graham A. W., McManus J. and Bernhard J. M., 2005. Anaerobic diagenesis of silica and carbon in continental margin sediments: Discrete zones of TCO2 production. *Geochim. Cosmochim. Acta* 69, 4611–4629.

Berg P., Røy H., Janssen F., Meyer V., Jørgensen B. B., Huettel M. and De Beer D., 2003. Oxygen uptake by aquatic sediments measured with a novel non-invasive eddy-correlation technique. *Mar. Ecol. Prog. Ser.* 261, 75–83.

Berg, P., Røy, H., Wiberg, P. L., 2007. Eddy correlation flux measurements: The sediment surface area that contributes to the flux. *Limnol. Oceanogr.* 52, 1672-1684.

Berner R. A., 1980. *Early Diagenesis: A Theoretical Approach*, Princeton University Press, Princeton.

Blackford J., Bull J. M., Cevatoglu M., Connelly D., Hauton C., James R. H., Lichtschlag A., Stahl H., Widdicombe S. and Wright I. C., 2015. Marine baseline and monitoring strategies for carbon dioxide capture and storage (CCS). *Int. J. Greenh. Gas Control* 38, 221–229.

Böttner C., Berndt C., Reinardy B. T. I., Geersen J., Karstens J., Bull J. M., Callow B. J., Lichtschlag A., Schmidt M., Elger J., Schramm B. and Haeckel M., 2019. Pockmarks in the Witch Ground Basin, Central North Sea. *Geochem., Geophys. Geosys*. 20, 1698–1719.

Boudreau B. P., 1997. Diagenetic models and their implementation., Springer-Verlag, Berlin.

Boudreau, B. P., 2001. Solute transport above the sediment-water interface. In *The Benthic boundary layer: Transport processes and biogeochemistry*, Oxford Univ. Press Oxford, UK, pp 104-126.

Brenner H., Braeckman U., Le Guitton M. and Meysman F. J. R., 2016. The impact of sedimentary alkalinity release on the water column CO2 system in the North Sea. *Biogeosciences* 13, 841–863.

Burdige D. J., 2006. Geochemistry of marine sediments. Princeton Univ. Press, Princeton, NJ.

Burdige D. J. and Komada T., 2011. Anaerobic oxidation of methane and the stoichiometry of remineralization processes in continental margin sediments. *Limnol. Oceanogr*. 56, 1781–1796.

Burdige D. J. and Komada T., 2013. Using ammonium pore water profiles to assess stoichiometry of deep remineralization processes in methanogenic continental margin sediments. *Geochem. Geophys. Geosys*. 14, 1626–1643.

Canfield D. E., 1993. Organic matter oxidation in marine sediments. In *Interactions of C, N, P and S Biogeochemical Cycles and Global Change*. Volume 4 of the series NATO ASI Series pp. 333–363.

Canfield D. E., Raiswell, R., Westrich, J. T., Reaves, C. M., Berner, R. A., 1986. The use of chromium reduction in the analysis of reduced sulfur in sediments and shales. *Chem. Geol.* 54, 149-155.

Canfield D. E., Jørgensen B. B., Fossing H., Glud R., Gundersen J., Ramsing N. B., Thamdrup B., Hansen J. W., Nielsen L. P. and Hall P. O. J., 1993. Pathways of organic carbon oxidation in three continental margin sediments. *Mar. Geol*. 113, 27–40.

Connelly, D., 2019. RRS James Cook Cruise JC180 25 April – 30 May 2019. *Strategies for the Environmental Monitoring of Marine Carbon Capture and Storage, STEMM-CCS*. National Oceanography Centre Cruise Report, No. 63, Southampton, 213pp.

Dale A. W., Bertics V. J., Treude T., Sommer S. and Wallmann K., 2013. Modeling benthic-pelagic nutrient exchange processes and porewater distributions in a seasonally-hypoxic sediment: evidence for massive phosphate release by Beggiatoa? *Biogeosciences* 10, 629–651.

Dale A. W., Sommer S., Lomnitz U., Montes I., Treude T., Liebetrau V., Gier J., Hensen C., Dengler M., Stolpovsky K., Bryant L. D. and Wallmann K., 2015. Organic carbon production, mineralisation and preservation on the Peruvian margin. *Biogeosciences* 12, 1537–1559.

Dale A. W., Flury S., Fossing H., Regnier P., Røy H., Scholze C. and Jørgensen B. B., 2019. Kinetics of organic carbon mineralization and methane formation in marine sediments (Aarhus Bay, Denmark). *Geochim. Cosmochim. Acta* 252, 159–178.

de Haas H, Boer W. and Van Weering T. C. E., 1997. Recent sedimentation and organic carbon burial in a shelf sea: the North Sea. *Mar. Geol*. 144, 131–146.

De Orte, M.R., Lombardi, A.T., Sarmiento, A.M., Basallote, M.D., Rodriguez-Romero, A., Riba, I., Valls, A.D., 2014. Metal mobility and toxicity to microalgae associated with acidification of sediments: CO_2 and acid comparison. *Mar. Environ. Res.* 96, 136–144

Diesing M., Kröger S., Parker R., Jenkins C., Mason C. and Weston K., 2017. Predicting the standing stock of organic carbon in surface sediments of the North – West European continental shelf. *Biogeochemistry* 135, 183–200.

Dixon, T., Romanak, K. D., 2015. Improving monitoring protocols for CO_2 geological storage with technical advances in CO_2 attribution monitoring. *Int. J. Greenh. Gas Control* 41, 29–42.

Eigaard, O.R., Bastardie, F., Breen, M., Dinesen, G. E., Hintzen, N. T., Laffargue, P., Mortensen, L. O., Rasmus Nielsen, J., Nilsson, H. C., O'Neill, F. G., Polet, H., Reid, D. G., Sala, A., Sköld, M., Smith, C., Sørensen, T. K., Tully, O., Zengin, M., Rijnsdorp, A. D., 2016. Estimating seabed pressure from demersal trawls, seines, and dredges based on gear design and dimensions. *ICES J. Mar. Sci*. 73, Supp. 1, i27–i43.

Emerson S., Jahnke R., Bender M., Froelich P., Klinkhammer G., Bowser C. and Setlock G., 1980. Early diagenesis in sediments from the eastern equatorial Pacific, I. Pore water nutrient and carbonate results. *Earth Planet. Sci. Lett*. 49, 57–80.

Flury S., Røy H., Dale A. W., Fossing H., Tóth Z., Spiess V., Jensen J. B. and Jørgensen B. B., 2016. Controls on subsurface methane fluxes and shallow gas formation in Baltic Sea sediment (Aarhus Bay, Denmark). *Geochim. Cosmochim. Acta* 188, 297–309.

Froehlich P. N., Klinkhammer G. P., Bender M. L., Luedtke N. A., Heath G. R., Cullen D., Dauphin P., Hammond D., Hartman B. and Maynard V., 1979. Early oxidation of organic matter in pelagic sediments of the eastern equatorial Atlantic: suboxic diagenesis. *Geochim. Cosmochim. Acta* 43, 1075–1090.

Grasshoff K., Kremlingl K. and Ehrhardt M., 1999. *Methods of Seawater Analysis*. Wiley-VCH, Weinheim., Weinheim.

Holmkvist L., Ferdelman T. G. and Jørgensen B. B., 2011. A cryptic sulfur cycle driven by iron in the methane zone of marine sediment (Aarhus Bay, Denmark). *Geochim. Cosmochim. Acta* 75, 3581–3599.

Holtappels M., Glud R. N., Donis D., Liu B., Hume A., Wenzhöfer F. and Kuypers M. M. M., 2013. Effects of transient bottom water currents and oxygen concentrations on benthic exchange rates as assessed by eddy correlation measurements. *J. Geophys. Res. Ocean.* 118, 1157–1169.

IPCC, 2005. Special Report Carbon dioxide Capture and Storage. B Metz, O. Davidson, H. de Coninck, M. Loos and L. Meyer (Eds.) Cambridge University Press, UK. pp 431.

IPCC, 2014. Climate Change 2014*: Impacts, Adaptation, and Vulnerability. Part A: Global and Sectoral Aspects. Contribution of Working Group II to the Fifth Assessment Report of the Intergovernmental Panel on Climate Change*. Cambridge University Press, Cambridge, United Kingdom and New York, NY, USA.

IPCC, 2018.: Summary for Policymakers. In: *Global Warming of 1.5°C. An IPCC Special Report on the impacts of global warming of 1.5°C above pre-industrial levels and related global greenhouse gas emission pathways, in the context of strengthening the global response to the threat of climate change, sustainable development, and efforts to eradicate poverty* [Masson-Delmotte, V., P. Zhai, H.-O. Pörtner, D. Roberts, J. Skea, P.R. Shukla, A. Pirani, W. Moufouma-Okia, C. Péan, R. Pidcock, S. Connors, J.B.R. Matthews, Y. Chen, X. Zhou, M.I. Gomis, E. Lonnoy, T. Maycock, M. Tignor, and T. Waterfield (eds.)]. World Meteorological Organization, Geneva, Switzerland, 32 pp.

Ivanenkov, V.N., Lyakhin, Y.I., 1978. Determination of total alkalinity in seawater. In: Bordovsky, O.K., Ivanenkov, V.N. (Eds.), *Methods of Hydrochemical Investigations in the Ocean* (in Russian). Nauka Publ. House, Moscow, pp. 110–114.

Jørgensen B. B., 1978. A comparison of methods for the quantification of bacterial sulfate reduction in coastal marine sediments II. Calculation from mathematical models. *Geomicrobiol. J.* 1, 29–47.

Jørgensen B. B. and Parkes R. J., 2010. Role of sulfate reduction and methane production by organic carbon degradation in eutrophic fjord sediments (Limfjorden, Denmark). *Limnol. Oceanogr*. 55, 1338–1352.

Jørgensen B. B., Findlay A. J. and Pellerin A., 2019. The biogeochemical sulfur cycle of marine sediments. *Front. Microbiol*. 10: 849, doi: 10.3389/fmicb.2019.00849.

Judd, AG, Long, D, and Sankey, M, 1994. Pockmark formation and activity, UK block 15/25, North Sea. *Bull. Geolog. Soc. Denmark*, 41, 34–49.

LaRowe D. E. and Van Cappellen P., 2011. Degradation of natural organic matter: A thermodynamic analysis. *Geochim. Cosmochim. Acta* 75, 2030–2042.

Lessin G., Artioli Y., Queirós A.M., Widdicombe S., Blackford J.C., 2016. Modelling impacts and recovery in benthic communities exposed to localised high CO_2. *Mar. Poll. Bull.* 109, 267-280.

Lichtschlag A., James R. H., Stahl H. and Connelly D., 2015. Effect of a controlled sub-seabed release of CO2 on the biogeochemistry of shallow marine sediments, their pore waters, and the overlying water column. *Int. J. Greenh. Gas Control* 38, 80–92.

Linke, P. Haeckel., 2018. *RV POSEIDON Fahrtbericht / Cruise Report POS518. Baseline Study for the Environmental Monitoring of Subseafloor* CO_2 *Storage Operations. Leg 1: Bremerhaven – Bremerhaven (Germany) 25.09.-11.10.2017, Leg 2: Bremerhaven – Kiel (Germany) 12.10.-28.10.2017.* GEOMAR Report N. Ser. 040, GEOMAR Helmholtz-Zentrum für Ozeanforschung, Kiel, 84 pp. DOI 10.3289/GEOMAR_REP_NS_40_2018.

Long, D, 1992. Devensian Late-glacial gas escape in the central North Sea. *Cont. Shelf Res*., 12, 1097–1110.

Luff R. and Moll A., 2004. Seasonal dynamics of the North Sea sediments using a three-dimensional coupled sediment-water model system. *Cont. Shelf Res.* 24, 1099–1127.

Mackenzie F. T. and Garrels R. M., 1966. Chemical mass balance between rivers and oceans. *Am. J. Sci*. 264, 507–525.

Marinelli R. L., Jahnke R. A., Craven D. B., Nelson J. R. and Eckman J. E., 1998. Sediment nutrient dynamics on the South Atlantic Bight continental shelf. *Limnol. Oceanogr.* 43, 1305–1320.

Mayer L. M., 1994. Relationships between mineral surfaces and organic carbon concentrations in soils and sediments. *Chem. Geol*. 114, 347–363.

McGinnis D. F., Sommer S., Lorke A., Glud R. N. and Linke P., 2014. Quantifying tidally driven benthic oxygen exchange across permeable sediments: An aquatic eddy correlation study. *J. Geophys. Res. Ocean*. 119, 6918–6932.

Megonigal J. P., Hines M. E. and Visscher P. T., 2004. Anaerobic metabolism: Linkages to trace gases and aerobic processes. In *Treatise on Geochemistry* (ed. W. H. Schlesinger). Elsevier-Pergamon, Oxford, UK. pp. 317–424.

Mesher, T., McNeill, C. L., Rühl, S., Widdicombe, S., 2020. Benthic biota characterisation in the vicinity of the Goldeneye platform during POSEIDON cruise POS527. PANGAEA, https://doi.org/10.1594/PANGAEA.910594

Meyers P. A., 1994. Preservation of elemental and isotopic source identification of sedimentary organic matter. *Chem. Geol.* 114, 289–302.

Michalopoulos P. and Aller R., 1995. Rapid clay mineral formation in Amazon delta sediments: Reverse weathering and oceanic elemental cycles. *Science* 270, 614–617.

Middelburg J. J., 1989. A simple rate model for organic matter decomposition in marine sediments. *Geochim. Cosmochim. Acta* 53, 1577–1581.

Poulton S. W. and Canfield D. E., 2005. Development of a sequential extraction procedure for iron: Implications for iron partitioning in continentally derived particulates. *Chem. Geol*. 214, 209–221.

Redfield, A. C., Ketchum, B. H., Richards, F. A., 1963. The influence of organisms on the composition of seawater. In: Hill, M.N. (Ed.), *The Sea, Vol. 2*. Wiley-Interscience, New York, pp. 26–77.

Røy H, Weber H. S., Tarpgaard I. H., Ferdelman T. G., Jørgensen B. B., 2014. Determination of dissimilatory sulfate reduction rates in marine sediment via radioactive ^{35}S tracer. *Limnol. Oceanogr. Methods* 12, 196-211.

Scholz, F., Hensen, C., Schmidt, M., Geersen, J., 2013. Submarine weathering of silicate minerals and the extent of pore water freshening at active continental margins. *Geochim. Cosmochim. Acta* 100, 200 – 216.

Schulz H. D., 2000. Quantification of early diagenesis: Dissolved constituents in marine pore water. In *Marine Geochemistry* (eds. H. D. Shulz and M. Zabel). Springer. pp. 85–128.

Schmidt, M., 2019. *RV POSEIDON Fahrtbericht / Cruise Report POS534 STEMM-CCS: Strategies for Environmental Monitoring of Marine Carbon Capture and Storage Leg 1: Kiel (Germany) – Aberdeen (United Kingdom) 01.05. – 22.05.2019 Leg 2: Aberdeen (United Kingdom) – Bremerhaven (Germany) 23.05.*

– *29.05.2019*. GEOMAR Report, N. Ser. 052 . GEOMAR Helmholtz-Zentrum für Ozeanforschung, Kiel, Germany, 51 pp. DOI 10.3289/geomar_rep_ns_52_2019.

Shell, 2014. Peterhead CCS project: Offshore Environmental statement. Shell, Aberdeen, 593pp.

Sommer S., Gier J., Treude T., Lomnitz U., Dengler M., Cardich J. and Dale A. W., 2016. Depletion of oxygen, nitrate and nitrite in the Peruvian oxygen minimum zone cause an imbalance of benthic nitrogen fluxes. *Deep-Sea Res. I* 112, 113–122.

STEMM-CCS project consortium, 2020. Strategies for Environmental Monitoring of Marine Carbon Capture and Storage: Research Highlights, 36 pages. doi.10.5281/zenodo.3627036

Taylor P., Lichtschlag A., Toberman M., Sayer M. D. J., Reynolds A., Sato T. and Stahl H., 2015. Impact and recovery of pH in marine sediments subject to a temporary carbon dioxide leak. *Int. J. Greenh. Gas Control* 38, 93–101.

Thamdrup B., Fossing H. and Jørgensen B. B., 1994. Manganese, iron, and sulfur cycling in a coastal marine sediment, Aarhus Bay, Denmark. *Geochim. Cosmochim. Acta* 58, 5115–5129.

Thullner M., Dale A. W. and Regnier P., 2009. Global-scale quantification of remineralization pathways in marine sediments: A reaction-transport modeling approach. *Geochem. Geophys. Geosyst.* 10, Q10012, doi:10.1029/2009GC002484.

Van Cappellen P. and Wang Y., 1996. Cycling of iron and manganese in surface sediment: A general theory for the coupled transport and reaction of carbon, oxygen, nitrogen, sulfur, iron, and manganese. *Am. J. Sci.* 296, 197–243.

Wallmann K., Aloisi G., Haeckel M., Tishchenko P., Pavlova G., Greinert J., Kutterolf S. and Eisenhauer A., 2008. Silicate weathering in anoxic marine sediments. *Geochim. Cosmochim. Acta* 72, 2895–2918.

Wallmann K., Haeckel M., Linke P., Haffert L., Schmidt M., Bünz S., James R., Hauton C., Tsimplis M., Widdicombe S., Blackford J., Queiros A. M., Connelly D., Lichtschlag A., Dewar M., Chen B., Baumberger T., Beaubien S., Vercelli S., Proelss A., Wildenborg T., Mikunda T., Nepveu M., Maynard C., Finnerty S., Flach T., Ahmed N., Ulfsnes A., Brooks L., Moskeland T., Purcell M., 2015. Best Practice Guidance for Environmental Risk Assessment for offshore CO_2 geological storage, ECO_2 Deliverable D14.1, 53 p., DOI: 10.3289/ECO2_D14.1

Wilczak, J. M; Oncley, S. P., Stage, S. A., 2001. Sonic anemometer tilt correction algorithms. *Bound.-Layer Meteorol.* 99, 127-150.

Zeebe, R.E., Wolf-Gladrow, D., 2001. *CO_2 in seawater: equilibrium, kinetics, isotopes*. 2nd edition. Elsevier Oceanography Series, vol. 65. 346 pp.